UNIVERSIDADE FEDERAL DE MINAS GERAIS

Instituto de Ciências Exatas

Programa de Pós-Graduação em Física

Nícolas Paulo Pereira Vasconcelos

A Wavelet-based method to enhance spectroscopic contrast in STM Images

Belo Horizonte
2023

Nícolas Paulo Pereira Vasconcelos

A Wavelet-based method to enhance spectroscopic contrast in STM Images

Dissertation presented to the Graduate Physics Program at Universidade Federal de Minas Gerais as a partial requirement for obtaining the Master's degree in Physics

Supervisor: Prof. Dr. Ângelo Malachias de Souza

Co-Supervisor: Prof. Dr. Rogério Magalhães Paniago

Belo Horizonte
2023

UNIVERSIDADE FEDERAL DE MINAS GERAIS
INSTITUTO DE CIÊNCIAS EXATAS
PROGRAMA DE PÓS-GRADUAÇÃO EM FÍSICA

ATA DE DEFESA DE DISSERTAÇÃO

ATA DA SESSÃO DE ARGUIÇÃO DA 709ª DISSERTAÇÃO DO PROGRAMA DE PÓS-GRADUAÇÃO EM FÍSICA, DEFENDIDA POR NÍCOLAS PAULO PEREIRA VASCONCELOS, orientado pelo professor Ângelo Malachias de Souza e coorientado pelo professor Rogério Magalhães Paniago, para obtenção do grau de **MESTRE EM FÍSICA**. Às 15 horas de seis de outubro de 2023, por videoconferência, reuniu-se a Comissão Examinadora, composta pelos professores **Ângelo Malachias de Souza** (Orientador - Departamento de Física/UFMG), **Rogério Magalhães Paniago** (Coorientador - Departamento de Física/UFMG), **Lívia Siman Gomes** (Departamento de Física/UFMG) e **Karolline Aparecida de Souza Araújo** (Instituto Federal de Educação, Ciência e Tecnologia de Minas Gerais) para dar cumprimento ao Artigo 37 do Regimento Geral da UFMG, submetendo o bacharel **NÍCOLAS PAULO PEREIRA VASCONCELOS** à arguição de seu trabalho de dissertação, que recebeu o título de **"A Wavelet-based method to enhance spectroscopic contrast in STM Images"**. O candidato fez uma exposição oral de seu trabalho durante aproximadamente 50 minutos. Após esta, os membros da comissão prosseguiram com a sua arguição e apresentaram seus pareceres individuais sobre o trabalho, concluindo pela aprovação do candidato.

Belo Horizonte, 06 de outubro de 2023.

Prof. Ângelo Malachas de Souza
Orientador do aluno
Departamento de Física/UFMG

Prof. Rogério Magalhães Paniago
Coorientador do aluno
Departamento de Física/UFMG

Profa. Lívia Siman Gomes
Departamento de Física/UFMG

Profa. Karolline Aparecida de Souza Araújo
Instituto Federal de Educação, Ciência e Tecnologia de Minas Gerais

Candidato: Nícolas Paulo Pereira Vasconcelos

Documento assinado eletronicamente por **Nícolas Paulo Pereira Vasconcelos**, **Usuário Externo**, em 09/10/2023, às 20:04, conforme horário oficial de Brasília, com fundamento no art. 5º do Decreto nº 10.543, de 13 de novembro de 2020.

Documento assinado eletronicamente por **Angelo Malachias de Souza**, **Membro de comissão**, em 10/10/2023, às 09:49, conforme horário oficial de Brasília, com fundamento no art. 5º do Decreto nº 10.543, de 13 de novembro de 2020.

Documento assinado eletronicamente por **Livia Siman Gomes**, **Professora do Magistério Superior**, em 10/10/2023, às 14:07, conforme horário oficial de Brasília, com fundamento no art. 5º do Decreto nº 10.543, de 13 de novembro de 2020.

Documento assinado eletronicamente por **Rogerio Magalhaes Paniago**, **Professor do Magistério Superior**, em 11/10/2023, às 12:17, conforme horário oficial de Brasília, com fundamento no art. 5º do Decreto nº 10.543, de 13 de novembro de 2020.

A autenticidade deste documento pode ser conferida no site https://sei.ufmg.br/sei/controlador_externo.php?acao=documento_conferir&id_orgao_acesso_externo=0, informando o código verificador **2701725** e o código CRC **C2BE503B**.

Referência: Processo nº 23072.261828/2023-99   SEI nº 2701725

Acknowledgements

Resumo

Nanoestruturas são objetos físicos com grande razão superfície/volume, com uma ou mais dimensões na escala nanométrica. Um importante exemplo dessas estruturas são os materiais bidimensionais, como o Grafeno, Bi_2Te_3, CeO_2, etc. Com uma amostra de Óxido de Cério em substrato de HOPG obtida por deposição por laser pulsado (PLD) é possível observar nanoestruturas. Através de técnicas que utilizam o Microscópio de Tunelamento por Varredura (STM) em determinadas tensões é possível obter imagens das respectivas nanoestruturas a uma específica condição de densidade de estados local. Isso nos permite estudar os fenômenos eletrônicos do material e suas interações com o substrato.

Através do uso de técnicas de filtragem e processamento de imagem, tais como Wavelets e Transformadas de Fourier, é possível melhorar significativamente a qualidade de imagens de nanoestruturas, permitindo que um estudo mais aprofundado das características de superfície seja realizado. Essa melhoria é crucial já que pode ser utilizada para aumentar o contraste de respostas eletrônicas/magnéticas/eletrostáticas em imagens de STM e AFM (Microscópio de Força Atômica).

Nesse trabalho utilizamos técnicas de processamento de sinal baseadas em wavelets para aumentar contraste eletrônico em nanoestruturas de óxido de cério observadas utilizando STM, assim como uma análise do tratamento realizado. Um script desenvolvido usando MATLAB, que trata automaticamente um grande número de imagens de STM e AFM usando decomposição por Wavelet, será discutido e analisado. Especial destaque é dado à melhoria de contraste nas imagens.

Palavras-chave: wavelet, microscopia/espectroscopia de tunelamento, processamento de dados, processamento de imagens, nanoestruturas, CeO_2, propriedades eletrônicas.

Abstract

Nanostructures are physical objects with a large surface/volume ratio, with one or more dimensions in the nanometer scale. An important example of these structures is the bidimensional materials, such as Graphene, Cerium Oxide, etc. Using a cerium oxide sample in HOPG substrate, obtained by pulsating laser deposition (PLD), it is possible to observe nanostructures. Using Scanning Tunneling Microscope (STM) techniques at selected bias we are able to obtain images of these nanostructures at a specific local density of state condition. This allows us to study the electronic phenomena and interactions with the substrate.

Through the use of image processing and filtering techniques, such as Wavelet and Fourier transforms, it is possible to significantly improve the quality of the images obtained, allowing a deeper study of surface features to be done. This improvement is crucial since it may be used to enhance the contrast of electronic/magnetic/electrostatic response in STM and Atomic Force Microscope (AFM) images.

In this work I will depict processed images of cerium oxide nanostructures using STM, as well as an analysis of the treatment performed. A script developed using MATLAB, automatically treating a large number of STM and AFM images using Wavelet decomposition, will be discussed and analyzed. Particular emphasis is given to improvements on image quality and contrast.

Keywords: wavelet, scanning tunneling microscopy/spectroscopy, data processing, image processing, nanostructures, CeO_2, electronic properties.

Table of Contents

1. INTRODUCTION

The development of quantum mechanics allowed the discovery of the wave-particle dualism, and one of the most exciting consequences of this idea is the tunneling effect. This effect occurs when a particle, generally an electron, passes through a potential barrier with higher energy than its own. This effect led to the invention of the Scanning Tunneling Microscope (STM) by H. Rohrer and G. Binnig in 1981 [30], an equipment that originated some of the most important experimental techniques on surface science.

The STM consists of a conductive and atomically sharp tip (usually made of Tungsten or Platinum Iridium alloy) which is set to approach a sample using a fine feedback system monitored by electronics capable of measuring a few pico-amperes. By slowly approaching the conductive tip of the surface under an applied bias one expects that an electric current will appear before physical contact is attained. Such a potential difference causes a leveling of the fermi energy level of the tip in relation to the sample at their closest point, allowing the tunneling current to flow. Such current value decays exponentially for increasing tip-surface distances, providing an extremely sensitive current setpoint that is used to monitor the distance between the tip and the sample [31, 32].

STM is, by these characteristics, a powerful tool to study and characterize the surfaces of different material classes such as 2D materials [1, 33, 34], topological insulators [35, 36], metals [34, 37] and semiconductors [1, 38]. With such a sensitive dependence on distance it is possible to infer and reconstruct with precision the topography of a sample down to its atomistic arrangement. In addition to microscopy, it is possible to study the local electronic structure of a given surface by using a technique known as Scanning Tunneling Spectroscopy (STS). STS allows one to retrieve direct information on how the local density of electronic states (LDOS) varies spatially as a function of the electron energy.

On the other hand, STM sensitivity is often a drawback since it is subjected to various sources of noise that can affect the quality and accuracy of both microscopy and spectroscopy measurements. Some of the most common types of noise are electronic noise, thermal noise, mechanical vibrations that may arise from the STM setup as well as from

external sources. To minimize these issues a number of precautions concerning STM installation and operation are set, including isolated electric grounding, vibration active and passive damping systems and precise temperature control [31, 32, 39, 34]. Nevertheless, whenever noise reduction in a given setup becomes limited, STM images can still be treated through signal processing methods [41].

Post-processing data treatment techniques involve filtering procedures applied to raw data in order to reduce noise while preserving desired information [42]. A key concept for noise reduction is the suppression of undesired frequencies of the STM current signal. However, those frequencies are usually invisible in the spatial domain where topographical or electronic information from an image is commonly represented. It therefore becomes mandatory to transit between the spatial domain and the frequency domain. This latter is understood through the representation of an image in terms of its frequency components. Such a representation often has explicit relations that are not observed straightforward in the spatial domain, such as periodic dependance or a specific type of noise at a defined frequency present in the whole image. To transit between the spatial and the frequency domain Fourier Transform became a very common tool. The Fourier Transform applied to a signal will decompose it in terms of periodic functions such as sines and cosines that are not spatially limited. Since STM signals are usually discrete datasets, the Fast Fourier Transform (FFT) is a standard tool in the area. Another important method related to frequency decomposition and much less explored in this field is the Wavelet Decomposition.

Wavelets are localized wave-like functions with finite extent and average value of zero [2, 3]. The wavelet decomposition consists in breaking up a signal into shifted and scaled versions of the original wavelet function. Therefore, the original signal is written as a function of these shifted and scaled wavelets, chosen among some known functions to perform the decomposition process [4, 5]. This approach carries some advantages when compared to Fourier Transform, such as conservation of the temporal information and the large variety of functions to choose in order to adapt better to a particular signal. Since Wavelets are localized functions, Wavelet Decomposition is a promising method to reduce or suppress non-periodic noise [10, 11, 12]. This process also can additionally isolate and remove undesired frequencies such as white noise and other non-regular artifacts.

Due to the reasons discussed above, STM images are suitable candidates to use Wavelet Decomposition in order to reduce noise and extract information from the LDOS. In order to study this application, a sample of Cerium Oxide on Highly Ordered Pyrolytic Graphite (HOPG) was chosen. The Cerium Oxide is deposited through pulsed laser deposition (PLD) and form triangular shaped nanostructures.

Cerium Oxide is a suitable choice since there is a weak contrast between the nanostructures and the HOPG substrate. Another interesting contrast observed is related to images at different tensions. This contrast is of fundamental importance since it possibly originates from electronic/magnetic/electrostatic responses. In order to enhance these weak contrasts, it is possible to use Wavelet based methods of noise reduction.

We study here how the Wavelet Decomposition can be used to reduce noise in different STM images. Several different wavelets were used in the decomposition and the best result (Symlet4) was chosen through trial and error. Automatic threshold values were determined for the images used. In order to provide an easy visualization of the method, a considerable part of the analysis in this work was made in two-dimensional profiles extracted from various STM images. Thus, the difference between images before and after the processing were evidenced. We use the MATLAB software to develop a code to implement these transforms. The code developed is capable of automatically processing a large number of STM images, with user-defined parameters such as wavelet used, level of decomposition and type of threshold detection (among others). The code is available in Appendix A.

2. SCANNING TUNNELING MICROSCOPY

Scanning Tunneling Microscopy (STM) is a probe-based imaging technique used to achieve high resolution images down to atomic scale. It has proven alongside few decades to be a powerful tool to understand the surface of different metallic or semiconductor compounds from distinct material classes such as 2D materials, topological insulators, transition metal dichalcogenides (TMDs), etc. STM has played a crucial role in surface science being used to characterize numerous emergent materials since its invention [1, 33-37, 43], becoming concomitantly a rare example of direct use of a quantum mechanical process - the Tunneling Effect - in a practical real-world application. The following sections provide a concise review of its most important characteristics and current use.

2.1 History

The Scanning Tunneling Microscope (see Fig. 2.1.1) was invented in 1981 by Gerd Binnig and Heinrich Rohrer (see Fig. 2.1.2) while they were working at IBM Zurich Research Laboratory [30]. The first experiment carried out with this method involved imaging the surface of a crystal of gold [44].
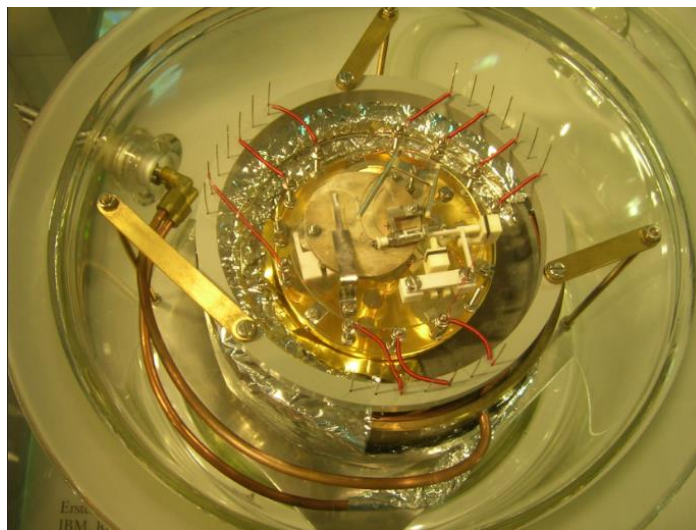

Fig 2.1.1 – The first Scanning Tunneling Microscope at the Deutsches Museum. Photo taken by J. Brew.

At the time STM was the pioneer technique among a new group of microscopy techniques called Scanning Probe Microscopy (SPM), that consist basically of monitoring how a tip probe interacts with a sample surface. In contrast to usual microscopy, SPM obtains information not by "seeing" (or using waves) but by "touching" the surface (physically interacting). The images obtained are inferences of the surface response obtained by very sensitive interactions between the probe and the material. This new approach of imaging allowed the study of materials on much smaller scales than before. The STM marked the history of physics given that, for the first time, humans could not only see, but also manipulate objects as small as individual atoms. The invention granted the Nobel Prize in Physics in 1986 and is regarded as the instrument that opened the door to nanotechnology with applications that span over a wide range of fields.

Fig. 2.1.2 – Gerd Binnig (left) and Heinrich Rohrer (right), inventors of the STM. Photo taken from the Nobel Foundation archive.

2.2 The Tunneling Effect

The Quantum Tunneling phenomenon takes place when a particle passes through a potential barrier despite having less energy than the barrier itself. It is a counterintuitive result, indeed, as there is no classical analogue and results in a classically forbidden

outcome. The effect arises as a consequence of wave properties that are intrinsic to small particles such as electrons.

A simple description can be drawn defining a square potential energy barrier, with potential energy:

$$U(x) = \begin{cases} 0, & x < -a \\ U_0, & -a < x < a \\ 0, & x > a \end{cases} \qquad . \tag{1}$$

Suppose then a particle beam that impinges the barrier with energy E, lower than the barrier's height U_0. The region between -a and a is then classically forbidden to a corpuscular particle. However, a quantum particle described by a wavefunction Ψ will be represented by eigenvalue equations given by [45]:

$$\begin{aligned} \frac{d^2\Psi_E(x)}{dx^2} &= q^2\Psi_E(x), \ |x| < a \\ \frac{d^2\Psi_E(x)}{dx^2} &= -k^2\Psi_E(x), \ |x| > a \end{aligned} \qquad . \tag{2}$$

Where Ψ_E is the energy eigenstate wave function and k and q are, respectively:

$$\begin{aligned} k &= \sqrt{\frac{2mE}{\hbar^2}} \\ q &= \sqrt{\frac{2m(U_0 - E)}{\hbar^2}} \end{aligned} \qquad . \tag{3}$$

In equation 3 $\hbar$ is the reduced Planck constant and m is the mass of the particle. Assuming that the particles are coming from the left, the general solutions to the problem assume the form:

$$\Psi_E(x) = \begin{cases} Ae^{ikx} + Be^{-ikx}, & x < -a \\ Ce^{qx} + De^{-qx}, & -a < x < a \\ Fe^{ikx}, & x > a \end{cases} \qquad . \tag{4}$$

This general solution provides an insight about the physical behavior of this particle in the forbidden region, where the function is either growing exponentially or decaying exponentially. In equation (4), the terms A, C and F represent beams of particles coming from the left, before the barrier, inside the barrier and after the barrier, respectively. The terms B and D represent beams of particles coming from the right, before the barrier and inside the barrier. The terms coming from the right represent the part of the incident beam that is reflected, and as in our system there is nothing to reflect the beam after the barrier, the sixth term (Ge⁻ⁱᵏˣ) was suppressed. To proceed the mathematical description, it is necessary to impose and apply boundary conditions to the solution, that must be continuous. Therefore:

$$\Psi(-a): Ae^{-ika} + Be^{ika} = Ce^{-qa} + De^{qa} \quad , \tag{5}$$

$$\left.\frac{d\Psi(x)}{dx}\right|_{x=-a} : ikAe^{-ika} - ikBe^{ika} = qCe^{-qa} - qDe^{qa} \quad , \tag{6}$$

$$\Psi(a): Ce^{qa} + De^{-qa} = Fe^{ika} \quad , \tag{7}$$

$$\left.\frac{d\Psi(x)}{dx}\right|_{x=a} : qCe^{qa} - qDe^{-qa} = ikFe^{ika} \quad . \tag{8}$$

Solving equation (7) and equation (8) for C and D in terms of F and replacing the solution into the equations (5) and (6) provides a way to eliminate C and D. After such solution step it is possible to solve equations (5) and (6) to obtain the ratios B/A and F/A. As F is the transmitted wave and A is the incident wave, the ratio F/A is the information necessary to obtain the transmission probability T:

$$T = \frac{|F|^2}{|A|^2} = \frac{1}{1 + \frac{(k^2+q^2)^2}{4k^2q^2} sinh^2(2aq)} \quad . \tag{9}$$

This is the probability for an incident particle, with less energy than the barrier's height, to pass through a barrier and emerge on the other side. This result is of tremendous importance, firstly because it indicates that in some cases the particle will in fact emerge

after the barrier. Secondly because the classical result for this phenomenon would lead to zero. The behavior of a wave function at the barrier is represented in Fig. 2.2.1. In this figure the width of the barrier is 2a, since it goes from -a to a. We can infer by equation (9) that as the barrier's depth increases, the transmission probability decreases.

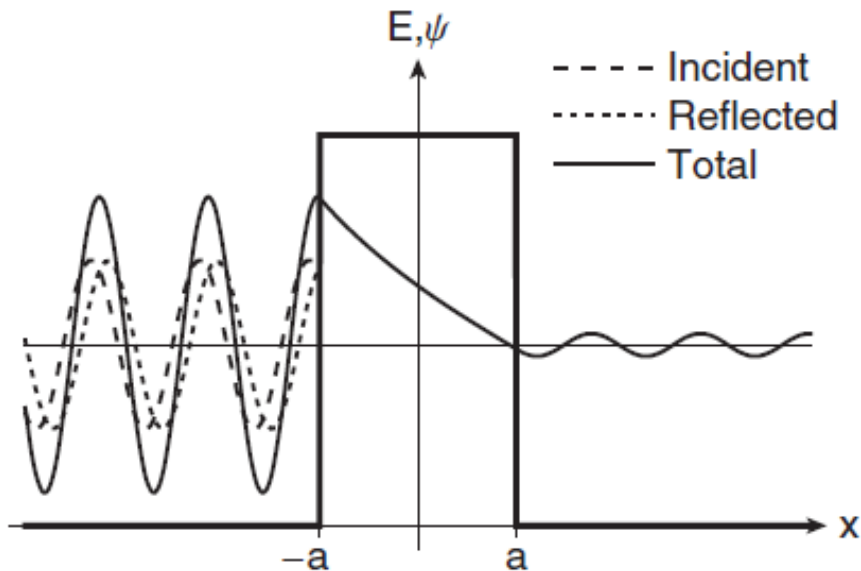**Fig. 2.2.1** – Wave function (real part) of a particle tunneling through a barrier. Figure taken from reference [45].

This effect is exactly what happens in the STM tip-sample system. The electrons in the tip will penetrate a potential barrier (air or vacuum) and will arrive at the sample or vice versa.
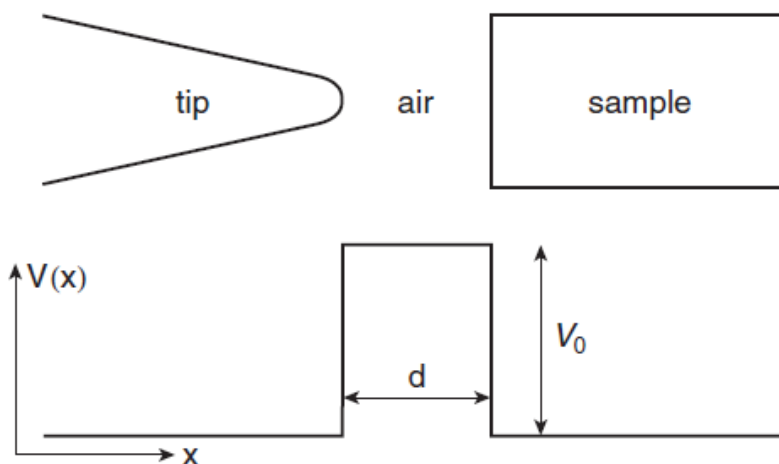

Fig. 2.2.2 – Schematic representation of the STM and the potential energy diagram. Figure taken from reference [45].

We can see in the Fig. 2.2.2 that the distance between the tip and the sample is related to the width of the potential barrier, therefore the transmission probability increases as the tip-sample distance decreases.

2.3 The Scanning Tunneling Microscope

Although the quantum tunneling phenomenon has been vastly studied before, it was not before the STM that this effect has been implemented in technology. Prior to discussing the key components present in Fig.2.3.1, it is important to state that the potential barrier between the tip and the sample in a STM can be either air or vacuum. Therefore, we can say that there are two major types of STM, the Air-STM and Ultra High Vacuum-STM (UHV-STM).
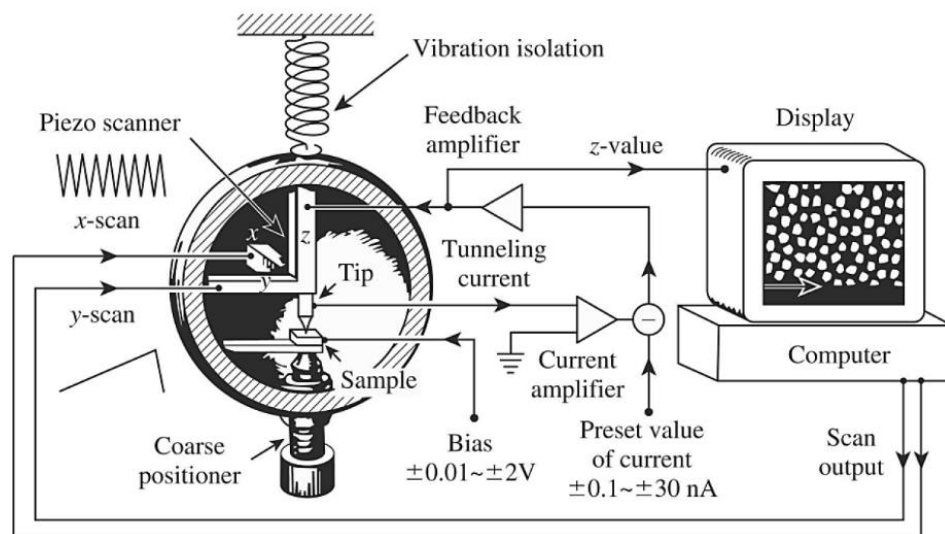
Fig. 2.3.1 – A detailed layout of the Scanning Tunneling Microscope. Figure taken from reference [31]

The first essential element for STM measurements is the probe tip. It needs to be conductive and atomically thin. The tip is usually made out of Tungsten (used in Vacuum conditions) or a Platinum-Iridium alloy (used in both vacuum and air condition). These are commonly used materials mainly due to their electrical conductivity, mechanical strength and smooth density of states. The Platinum-Iridium alloy is often chosen in Air-STM on account of its highly resistance to oxidation in air. Since there is reduced oxidation in vacuum, a tungsten tip is a better choice for UHV-STM, being only necessary to deoxidize the

tip by chemical or physical methods prior to its use in the vacuum environment. One of the most important reasons for the tungsten tip choice in vacuum is that it can be mechanically sharpened to a very fine point due to metallic grain cleavage, making it suitable for high-resolution imaging.

The probe tip is attached to a piezo-drive, a calibrated stage made of piezoelectric materials. Piezoelectric materials are characterized by their ability to generate electric charge in response to applied mechanical stress or vice-versa. This property allows the creation of devices that convert electrical charges in mechanical movements, called piezoelectric transducers. These transducers will expand or contract upon an applied voltage, resulting in controlled motion with picometric resolution (usually tens of pm). Equipped with these transducers in three directions, the STM is able to scan surfaces with extreme precision.

Finally, a feedback system based on a very sensitive amperemeter is mandatory. Since tunneling currents are usually in the range of nA to pA, it is necessary to monitor the tip-surface current with specially designed electric amplifiers that will dynamically control the height of the tip with respect to the studied surface. Images are usually carried out by setting a fixed bias and monitoring a current setpoint.

In order to start a measurement or image acquisition the tip is set to approach the sample slowly, until it reaches a distance of less than a nanometer. At this extremely short distance, the wavefunctions of electrons of the tip and the sample are overlapped. A bias voltage applied between sample and tip induces the flow of electrons, generating the tunneling current. Without the bias voltage, no current would appear as the fermi level of both tip and sample would be equal. To supply this system with electrons it is necessary to ground either the tip or the sample. By convention, the tip is usually grounded. If the tip is grounded, the bias voltage applied will be positive and applied to the sample. This will raise the fermi energy level of the tip in relation to the sample and allow the electrons of the tip to tunnel to unoccupied states in the sample. The tunneling current generated is in sub-nanoampere range.
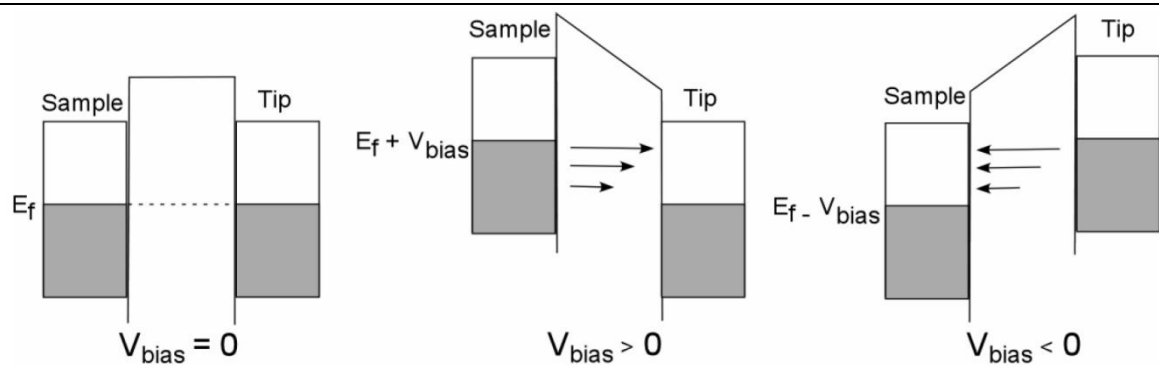
Fig. 2.3.2 – Schematic view of the fermi energy level of the tip and sample upon different bias voltage. Figure taken from reference [46].

STMs can operate in two distinct modes, constant current mode and constant height mode. In constant current mode, the tunneling current remains constant throughout the entire measurement. To ensure this, the z-axis piezo-drive adjusts its distance from the sample constantly. Since the tunneling current is extremely sensitive, even atomic size variations result in current change, therefore the tip can really follow the surface physical profile of the material. The information obtained changing the distance between the tip and sample is used to reconstruct the topography. In constant height mode, a fixed height is established, and the tip scans the surface measuring the fluctuations in current resulting from alterations in the sample's topography while the tip position is maintained fixed in the z-axis. The relation between the tunneling current and the tip-sample distance is known, and as before it is possible to reconstruct the topography. In both cases, a fine feedback system is used to precisely control the tip-sample distance. The feedback system works by setting a target value of current. This value is being continuously monitored and if it exceeds or falls below a predetermined threshold, the tip will either approach or retract from the sample. For example, in constant current mode, if the topography of the sample suddenly rises, the distance between the tip and the sample will shorten and the tunneling current will consequently increase. The feedback system quickly fixes it by withdrawing the tip and by this the current remains constant. Since STM measures currents, it is sensitive to local electronic variations in addition to topography variations. Therefore, it is fundamental to understand that the reconstructed image is a convolution of the topography of the sample and its local density of states (LDOS).

Another important component worth mentioning is the vibration isolation. The STM needs to be isolated from its surroundings to be able to achieve atomic resolution, given that the tip-sample distance to achieve tunneling is sub nanometer, any vibration that affect the system may cause the tip to hit the sample. To avoid this, it is common to use isolated electric grounding, vibration active and passive damping systems as well as placing the STM in a solid block isolated from the rest of the building.

2.4 Bardeen Theory

To gain a deeper insight into the functioning of the STM it is convenient to delve deeper in tunneling theories to study how the tunneling current responds. To accomplish this, we employ the Bardeen theory of tunneling, which will give us a more elaborate view about the absolute value of the tunneling current.

To begin, it is convenient to assume that the STM tip and sample are separated so that their electronic structure does not interact with each other. Therefore, we can consider their electronic structures separately. For the STM tip we have then [31, 47]:

$$i\hbar \frac{\partial \Psi}{\partial t} = \left[\frac{-\hbar}{2m} \frac{\partial^2}{\partial z^2} + U_T \right] \Psi \quad . \tag{10}$$

Where U_T is the potential function of the tip. Ψ depends on both time and spatial coordinates. The stationary states are [31, 47]:

$$\Psi = \psi_\mu e^{-iE_\mu t/\hbar} \quad . \tag{11}$$

The wavefunction and energy eigenvalues of the tip satisfies [31, 47]:

$$\left[\frac{-\hbar}{2m} \frac{\partial^2}{\partial z^2} + U_T \right] \psi_\mu = E_\mu \psi_\mu \quad . \tag{12}$$

All above apply to the wavefunction and energy eigenvalues of the sample as well, where U_s is its potential function, thus similar equations can be written to the sample. It is convenient to define a region z_0 in which the potential energy of the tip is zero, i.e., if $z > z_0$ then $U_s = 0$. This physically means that we consider that the potential energy of the sample only achieves relevant values near the sample surface, while it remains zero from the potential barrier beyond.

The wavefunction amplitude for both tip and sample decay exponentially in the vacuum barrier between them (as seen in equation (4)). However, as the tip approaches the sample, one gets closer to the onset of the tunneling regime and the tunneling current eventually starts to flow. This current is sensitive to both tip and sample potential, thus we represent this new state by [31, 47]:

$$ i\hbar \frac{\partial \Psi}{\partial t} = \left[\frac{-\hbar}{2m} \frac{\partial^2}{\partial z^2} + U_s + U_T \right] \Psi \qquad . \tag{13} $$

In the presence of the combination of both potentials, from the tip and from the sample, the state ψ_μ, previously described by equation (12), has now the probability of transferring an electron to the states of the sample. Therefore, we represent it as [31, 47]:

$$ \Psi = \psi_v^S e^{-iE_v^S t / \hbar} + \sum_{\mu=1}^{\infty} c_\mu(t) \psi_v^T e^{-iE_\mu^T t / \hbar} \qquad . \tag{14} $$

Where ψ_v^S and ψ_v^T are, respectively, the wavefunctions of the sample and the tip. The term $c_\mu(t)$ is a coefficient to be determined, related to the temporal dependency of the potential function of the tip. We assume firstly that $c_\mu(0) = 0$. One additional fundamental assumption of Bardeen's tunneling theory is that ψ_v^S and ψ_v^T are approximately orthogonal, i.e.:

$$ \int \psi_v^S * \psi_v^T d^3 r \cong 0 \qquad . \tag{15} $$

We can now combine equation (14) and equation (13) to obtain [31, 47]:

$$ i\hbar \sum_{\mu=1}^{\infty} \frac{dc_\mu(t)}{dt} \psi_\mu^T e^{-iE_\mu^T t/\hbar} = U_T \psi_\nu^S e^{-iE_\nu^S t/\hbar} + U_s \sum_{\lambda=1}^{\infty} c_\lambda(t) \psi_\lambda^T e^{-iE_\lambda^T t/\hbar} \qquad . \tag{16} $$

We neglect the second term on the right side since it is a second order infinitesimal quantity. We obtain then:

$$ i\hbar \frac{dc_\mu(t)}{dt} = \int_{z>z_0} \psi_\nu^S U_T \psi_\mu^T * e^{-i(E_\nu^S - E_\mu^T)t/\hbar} d^3\boldsymbol{r} \qquad . \tag{17} $$

If we define a tunneling matrix element as the follow [31, 47]

$$ M_{\nu\mu} \equiv \int_{z>z_0} \psi_\nu^S U_T \psi_\mu^T * d^3\boldsymbol{r} \qquad , \tag{18} $$

it is possible to obtain an explicit expression of the tunneling current. First by simply integrating equation (17), obtaining [31, 47]:

$$ c_\mu(t) = M_{\nu\mu} \frac{e^{-i(E_\nu^S - E_\mu^T)t/\hbar} - 1}{(E_\nu^S - E_\mu^T)} \qquad . \tag{19} $$

The probability of finding the μ-th state of the sample, starting with the ν-th state of the tip, i.e., the probability of an electron to populate the state ψ_μ^T is [31, 47]:

$$ p_{\nu\mu}(t) \equiv \left|c_\mu(t)\right|^2 = \left|M_{\nu\mu}\right|^2 \frac{4\sin^2[(E_\nu^S - E_\mu^T)t/2\hbar]}{(E_\nu^S - E_\mu^T)^2} \qquad . \tag{20} $$

This probability is maximum when $E_\nu^S = E_\mu^T$, in other words, the tunneling current depends on how many states near the energy value of a state in the tip into which the sample can effectively tunnel.

One important concept to introduce is the density of states. The density of states is the number of available quantum states per energy range in a system and we will refer to it as $\rho(E)$. This concept will be further discussed along the next chapter of this dissertation. Using the follow mathematical identity:

$$\int_{-\infty}^{\infty} \frac{sin^2 au}{\pi a u^2} \, du = 1 \qquad . \tag{21}$$

the probability of tip states that the sample can tunnel into is [31, 47]:

$$p_{\nu\mu}(t) = \frac{2\pi}{\hbar} \left| M_{\nu\mu} \right|^2 \rho_s(E_\nu^S) t \qquad . \tag{22}$$

We limit our study to the case where $E_\nu^S = E_\mu^T$. This condition is known as the condition of elastic tunneling [31]. This means that a state in the tip can only tunnel into states in the sample if both states are in the same energy. The number of available states in the tip is defined by its density of states and by the bias voltage V. Finally, the tunneling current is [31,47]:

$$I = \frac{2\pi e^2}{\hbar} \left| M_{\nu\mu} \right|^2 \rho_s(E_\nu^S) \rho_t(E_\mu^T) V \qquad . \tag{23}$$

where e is the elementary charge. Ultimately, we obtained the tunneling current in function of the density of states of both sample and tip, bias voltage and tunneling matrix element. This result is remarkable since it shows the importance of density of states to the tunneling current and consequently to the STM.

Last but not for least, it is worth mentioning the qualitative relation between the tunneling current and the tip-sample distance. This result comes from considering the density of states of the sample, at the Fermi edge [32]:

$$I \propto V_b \rho_s(E^S) e^{-2\sqrt{2m(U_0 - E)}z/\hbar} \qquad . \tag{24}$$

Remembering that U_0 is the height of the potential barrier, it is possible to see that the tunneling current decays exponentially with the tip-sample distance, as well as being linearly dependent on the density of states of the sample.

2.5 Scanning Tunneling Spectroscopy

Scanning Tunneling Spectroscopy (STS) is a complementary operation mode with respect to the imaging method, using the current-bias relation to infer local electronic properties at atomic scales, such as energy levels, density of states and local atomic interactions. The spectroscopic aspect of the STS involves measuring the tunneling current as a function of the bias voltage, i.e., while STM normally focus on topographic maps, STS focus on the tunneling conductance (defined as I/V) [46].

After the microscope enters the tunneling regime at a given bias in a given nanometric region, the bias voltage can be varied in a previously determined range to study how the tunneling current responds to the voltage. This primary electronic response is commonly used to classify materials as metals, semi-metals, semiconductors or insulators [1, 46, 47]. A remarkable characteristic of such methodology is that the STS is able to address the local density of states (LDOS) rather than the average density of states, since it relies on an atomically thin tip. The density of states refers to the density of available electronic states in a material, providing information about the energy distribution of electrons. In this particular case LDOS refers to the density of states at a very specific location within a material, usually limited laterally by a few nanometers [46]. Finally, since there is no physical contact between tip and sample, there is no need to consider Schottky barriers between the systems (absence of tip/sample contact interface).

The relation between the current and the LDOS can be shown in a simplified approach. We consider that the electrons on the tip and on the sample follow the Fermi-Dirac distribution ($f(E) = 1 + exp[(E - E_f)/k_bT]^{-1}$) [31]. The tunneling current can be evaluated by summing over all relevant states, and if k_bT is smaller than the energy resolution required in the measurement, Fermi distribution can be understood as a step function. The tunneling current is then given by [31]:

$$I = \frac{4\pi e}{\hbar} \int_0^{eV} \rho_s(E_\nu^S - eV + \varepsilon)\rho_t(E_\mu^T + \varepsilon)\left|M_{\nu\mu}\right|^2 d\varepsilon \qquad . \tag{25}$$

An assumption made by Bardeen is that the tunneling matrix elements do not change much in the interval of interest, thus [31]:

$$I \propto \int_0^{eV} \rho_s(E_\nu^S - eV + \varepsilon)\rho_t(E_\mu^T + \varepsilon)\, d\varepsilon \qquad . \tag{26}$$

Finally, the derivative of the current is:

$$\frac{dI}{dV} \propto \rho_s(E_\nu^S - eV)\rho_t(E_\mu^T) \qquad . \tag{27}$$

Equation (27) shows the normalized differential tunneling conductance, which is commonly used since its dependency on the density of states is simple and direct. The density of states of both tip and sample contributes equally to determine the tunneling current. With such results one can infer if there are local electronic variations at the surface and study changes in LDOS with respect to local chemical (clustering) or topographic (step edges, defects) fluctuations.

3. SIGNAL PROCESSING TECHNIQUES

In data processing and science in general a signal is any set of information that varies over time or space and can be measured. In summary, a signal can be seen as a function which describes a set of information about something. A data set of tunneling current measurements varying in function of the bias voltage is a signal, for example. In this case, the value of tunneling current depends only on the bias voltage, $I=f(V)$, therefore our function is a one-dimensional signal. There are countless examples of common one-dimensional signals, where the most important example in our scope is the topographic profile of a sample. This information can be extracted from an STM image (height in function of position in the x-axis).

Another good example of a signal is an image. An image consists in a matrix of values (pixels), each pixel storing a number related to brightness or intensity and located at a defined position in space (i.e., brightness varying spatially). However, to form a single image, we need to plot brightness information as a function of two position coordinates, $Im=f(x,y)$, indicating that an image is a two-dimensional function.

Signals can be categorized into two main types, continuous signals and discrete signals. As the nomenclature suggests, continuous signals vary continuously over a range of time or space, i.e., a function describing this signal has continuous domain and range. Discrete signals, on the other hand, consist in a discrete set of values, defined at specific points in time (sampling), i.e., a function with discrete time (or space) domain. A third and more recent type of signal, which has become common over the past decades and the most used type, is the digital signal, when the function has discrete time/space domain and intensity range. Due to the requirements to represent information in a computer, digital signals are much more common than continuous or discrete signals in signal processing. A landscape seen by a human eye is a good example of a continuous signal. However, if a photograph of the landscape is taken and transferred to a computer, the landscape will now be represented by pixels (discrete space domain), in which a discrete value of brightness will be assigned to each pixel (discrete intensity range). The landscape, now as a digital image,

will then be considered a digital signal. These signals are often obtained by sampling continuous signals at regular intervals, known as digitalization process (as mentioned above in the landscape example). Usually, a discrete dataset in both domain and range are enough to represent satisfactorily physical phenomena. STM data, for example, is represented through the use of digital signals [42].

Signals are, therefore, a primary and indispensable form of visualizing information. Nevertheless, the information may not be fully explicit. In the vast majority of the time, it will be necessary to extract meaningful information from data obtained in an experiment or measurement. For this demand, the signal processing area has quickly developed in the last decades, profiting of the increasing availability of computational resources. Signal processing's makes use of several techniques to improve data quality such as filtering, compression, amplification, noise removal, sharpening, etc. These tools have several important applications. For example, compression can be used to reduce the amount of storage required by a security camera, filtering and noise removal can be used to improve the camera's contrast quality. Signal processing plays a crucial role in various fields, including audio and video processing, image and speech recognition, biomedicine, experimental physics and others.
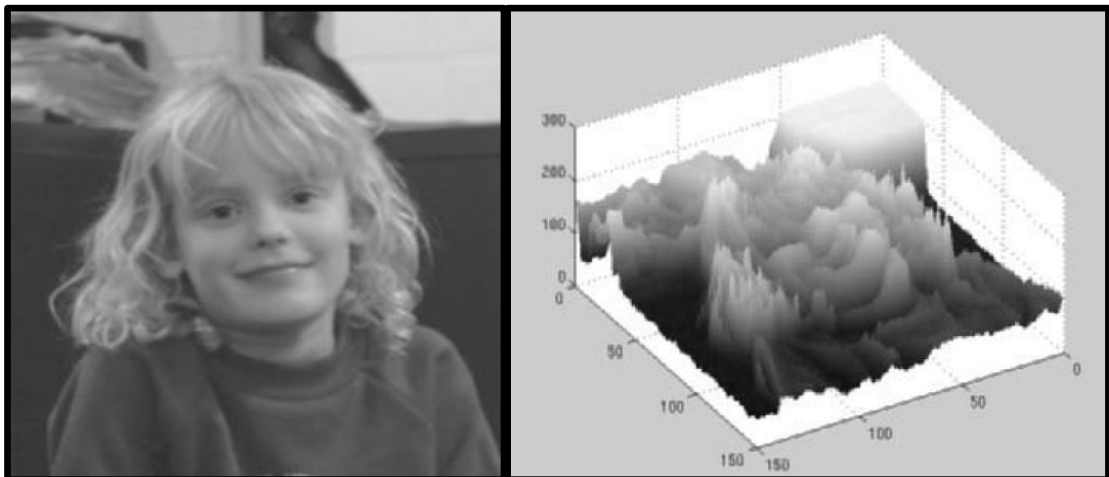

Fig. 3.1 – Two different representations of the same information. Figure adapted from reference [42]

One of the main gains in signal processing is the ability to extract and reorganize information. This ability is important given that the manner in which information is presented can be the determining factor in whether or not the reader comprehends it. In

Fig. 3.1, the image of a girl is represented in two distinct ways: in a conventional grayscale image and in a three-dimensional brightness map. In the photo on the left one can instantly interpret the image. However, in the photo on the right, comprehension is significantly impaired due to the manner in which the information was presented.

In terms of visualization, signals are commonly represented in three primary domains: the spatial domain, the frequency domain and the time domain. Each domain captures different aspects of the signal's characteristics. Spatial domain contains represents the spatial distribution of data. In the time domain, variations occur over time, representing how the data changes as time passes. In the frequency domain, information changes with frequency, revealing different components present in the data with intrinsic connection with either time or spatial domain. An STM image is an example for representation in spatial domain, as it represents height in terms of position. The light spectrum of a star is an interesting example for frequency domain representation, since it shows how intensity depends on the frequency of the light captured. Finally, an Electro-cardiogram is represented in time domain, given that it maps the heartbeat over time.

Each of these representations' explicit different characteristics of the original signal, being possible to choose the representation that best fits each case. There are tools that allow us to transit between different domains and one of the most fundamentals signal processing technique is the Fourier Transform (FT). FT is responsible for carrying out the transition from time or spatial domains to frequency representation.

3.1 Fourier Transform

The Fourier transform $\mathcal{F}$ is a mathematical process that converts a function, commonly time-dependent, into a frequency-dependent function. It is an integral (or summation) responsible for transposing discrete or continuous functions from the time domain to the frequency domain. It can be additionally understood as a linear operator that acts on a function resulting in another function, as shown below:

$$\mathcal{F}\{f(t)\} = F(\xi) \quad . \tag{28}$$

Where ξ is a frequency in Hertz. The continuous Fourier transform $\mathcal{F}$ is given by [42]:

$$\mathcal{F}\{f(t)\} = F(\xi) = \int_{-\infty}^{\infty} f(t)e^{-2\pi i \xi t}dt \quad , \tag{29}$$

and the inverse Fourier transform $\mathcal{F}^{-1}$ can be written as [42]:

$$\mathcal{F}^{-1}\{F(\xi)\} = f(t) = \int_{-\infty}^{\infty} F(\xi)e^{2\pi i \xi t}d\xi \quad . \tag{30}$$

In order to obtain a meaningful result from this operation, the function $f(t)$ needs to satisfy two main conditions. The first one is that the integral of $f(t)$ over the entire domain must be less than infinite, i.e., $\int_{-\infty}^{\infty} |f(t)|dt < \infty$. The second one is that $f(t)$ may have only a finite number of discontinuities in any finite interval. To better understand the meaning of these equations, it is convenient to express equation (30) as a Riemannian sum, as follow:

$$f(t) \doteq (\ldots + F(\xi_0)e^{2\pi i \xi_0 t} + F(\xi_1)e^{2\pi i \xi_1 t} + \ldots)\Delta\xi \quad . \tag{31}$$

Where $\Delta\xi = \xi_{k+1} - \xi_k$ for all k. Equation (31) demonstrates that it is possible to break down any function into a weighted combination of various complex exponentials. We remember from Euler's formula that:

$$e^{ix} = cos(x) + i\,sin(x) \quad . \tag{32}$$

Therefore, it is possible to decompose exponentials into sines and cosines. Consequently, decompose a function in terms of complex exponentials is equivalent to decompose this same function into sines and cosines components. This decomposition begins with a frequency ξ_0 and other frequencies are obtained multiplying ξ_0 by natural numbers. It may be noted that this representation consists in a Real and an Imaginary part, since the

coefficients ξ_k are often complex numbers, given both magnitude and phase of the wave. Because of that, we must procced with caution while dealing with the function $F(\xi)$ (frequency-dependency). Some common formulas to extract information from the frequency domain are [42]:

$$F(\xi) = Re\big(F(\xi)\big) + i\ Im\big(F(\xi)\big) \qquad , \tag{33}$$

$$|F(\xi)| = \sqrt{Re\big(F^2(\xi)\big) + Im\big(F^2(\xi)\big)} \qquad , \tag{34}$$

$$\phi(\xi) = arctan\big(Im\big(F(\xi)\big)/Re\big(F(\xi)\big)\big) \qquad . \tag{35}$$

Where $Re\big(F(\xi)\big)$ denotes the real part of the complex function, $Im\big(F(\xi)\big)$ denotes the imaginary part. The equations (33), (34) and (35) are used respectively to obtain the complex spectrum, amplitude spectrum and phase spectrum for a given function.

The Fourier Transform is also subject to the uncertainty principle, which states that is impossible to have a signal which is arbitrarily narrow in both time and frequency domains [42], i.e., 'signal duration' * 'Frequency bandwidth' $\geq \frac{1}{\pi}$.

In summary, the Fourier transform will provide weighted contributions of each frequency to form the original function, considering all frequency range. An example of some common functions and their respective Fourier transform can be seen in Fig. 3.1.1.
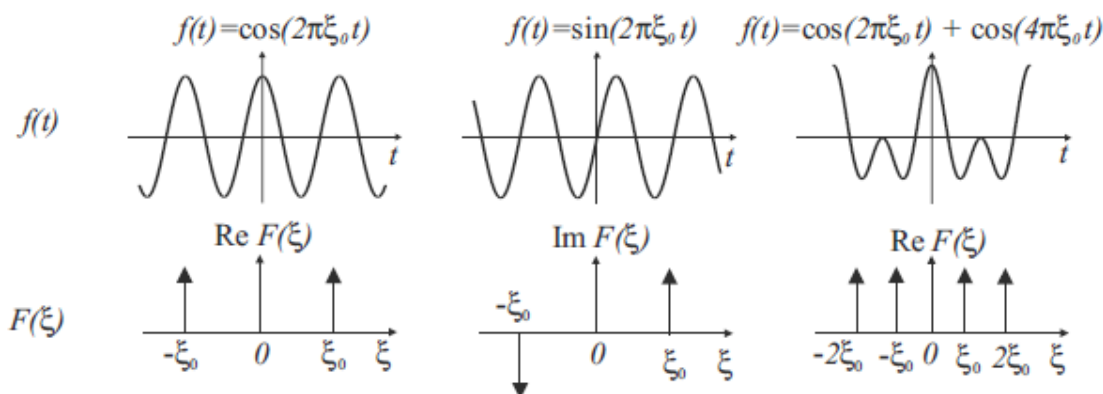

Fig. 3.1.1 – One-dimensional Fourier transform of different sinusoidal functions. Figure adapted from reference [42].

Studying the frequency domain of a function may evidence important information such as the existence of periodic relations, which can be crucial to solve a problem. A common application related to Fourier transform, while studying the frequency domain, is the implementation of filters [50]. In image processing, Fourier transforms has a wide spread use such as image compression, image analysis, image reconstruction, among others. Besides the many possible uses for this technique, it is worth mentioning the analysis of STM [49] and AFM [48] images. The Fourier transform is therefore one of the most fundamental techniques in the field of signal processing.

Equation (29) is a continuous representation for a Fourier transform. However, it is not straightforward to use it to study a digital signal. As computers deal with discrete signals, it becomes necessary to get around it and use an adapted version of this linear operator called discrete Fourier transform.

3.1.1 Discrete Fourier Transform

The Discrete Fourier transform (DFT) is given by a summation with the form

$$F(k) = \frac{1}{N} \sum_{n=0}^{N-1} f(n) e^{(-2\pi i \frac{nk}{N})} \quad , \tag{36}$$

and its inverse

$$f(n) = \frac{1}{N} \sum_{n=0}^{N-1} F(k) e^{(2\pi i \frac{nk}{N})} \quad . \tag{37}$$

Where the spectrum F(k) is periodically extended with period N. This alternate version of the Fourier transform can be used to analyze digital signals in a computer and is usually implemented by most of data analysis softwares. However, it is important to mention that besides the technique implementation through computer, the processing time must be

taken into account. This issue led to the development of an alternative algorithm known as Fast Fourier Transform (FFT). The FFT quickly became very popular, becoming one of the most used methods to implement Fourier transform.

To further illustrate this discussion, suppose a function $f(t) = sin(2\pi\nu_1 t) + sin(2\pi\nu_2 t)$. This is easily created using MATLAB. The function $f(t)$ is a wave composed by two pure frequencies ν_1 and ν_2. If we use FFT in function $f(t)$ it is expected to find clear peaks at the two main frequencies that make up the signal. It is possible to observe the exactly expected result in Fig.3.1.2 for $\nu_1 = 2$Hz and $\nu_2 = 1Hz$.
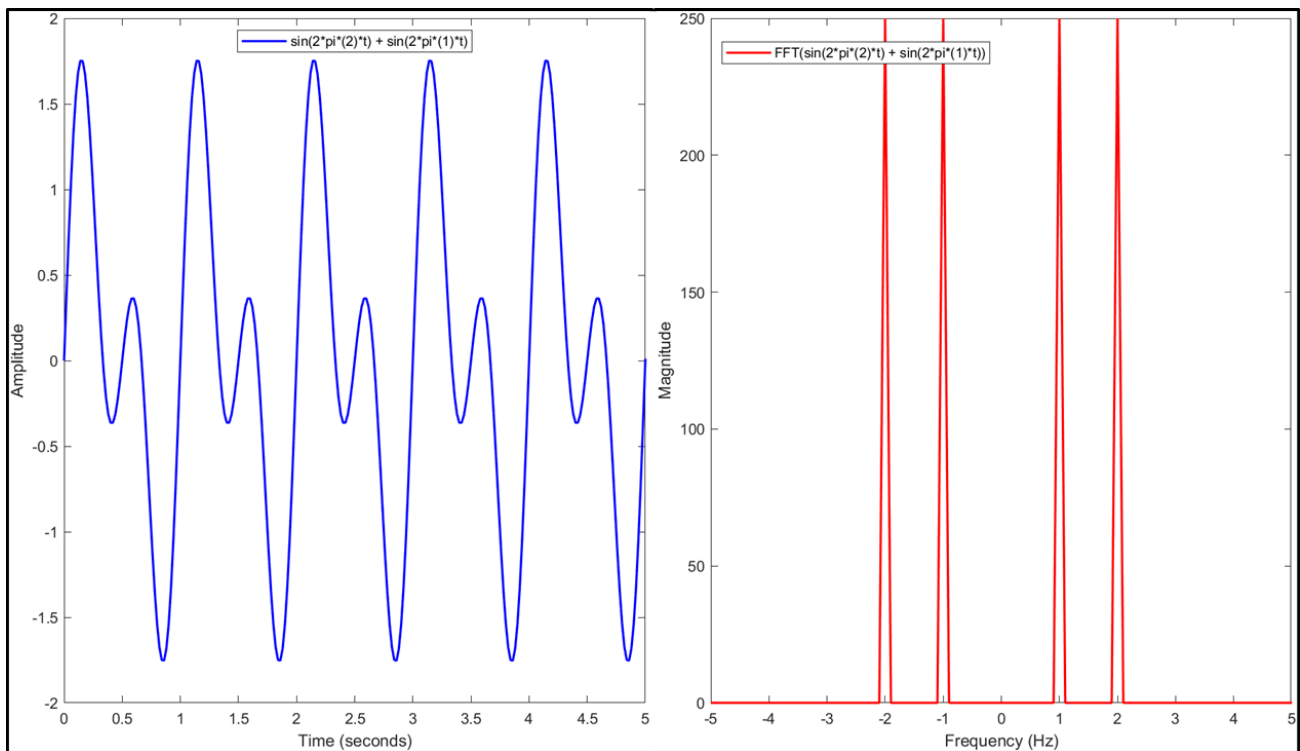

Fig. 3.1.2 – The graph of the function $f(t) = sin(2\pi\nu_1 t) + sin(2\pi\nu_2 t)$ with $\nu_1 = 2$Hz and $\nu_2 = 1Hz$ in blue. The graph in red is the Fast Fourier Transform of function $f(t)$. This figure was using MATLAB.

It is important to mention that this is a reversible process. After transitioning to the frequency domain one can apply the inverse transform to return to the original function. With this characteristic it is possible to make use of a technique that acts on specific frequencies such as a mask or a filter, and then return to the original signal.

Another important consideration is that the paragraphs above refer to the one-dimensional Fourier transform. The two-dimensional Fourier transform is simply a

generalization of the one-dimensional case. However, a very interesting result is obtained from the interpretation of the two-dimensional case. For the one-dimensional case the only independent variable is the time *t.* For the two-dimensional case the initial function depends on two variables. In signal processing, these variables are usually x and y, representing a pixel position on a plane. The variables associated with the resultant transform are referred to as spatial frequencies, which serve as the spatial counterparts to the familiar frequencies associated with time. Thus, it is possible to use it to study images.

Although very efficient, Fourier transform fails in some details. Inspite of its excellence for the exploration of global properties of a signal (frequency spectrum), it lacks phase specificity, meaning that the information of specific time values for the onset of each frequency is suppressed. The lost temporal information can be retrieved applying the inverse Fourier transform and returning to the temporal/spatial spectrum, however, time and frequency information cannot be held simultaneously. This happens mostly because Fourier transform decomposes functions in terms of non-localized waves such as sines and cosines. Using a similar technique supported by another class of waves, time-localized, solve this issue.

3.2 Wavelets

Wavelets were independently developed through history in different fields of science, such as signal processing, mathematics and physics, among others. However, the first mention of the term "wavelet" is credit to the Hungarian mathematician Alfréd Haar, presented in his thesis in 1909. The fundamental "Haar" wavelet was then named in his honor [2].

Wavelet transform appear as an alternative to Fourier transform, built to handle its limitations. Wavelets are a class of wave-like functions with finite extent and average value of zero. The finite time span is understood by initial and final amplitudes equal zero, meaning that these functions have well-defined beginning and end. This is a fundamental characteristic which differentiates wavelets from other periodic common functions such as sines or cosines. Finite extent means that the function is well localized in space. Due to the

wave nature and its property of locality, wavelets can be thought of as "brief oscillations".
Differently than sines or cosines, wavelets are able to provide localization in space at a
certain level, although it is not possible to obtain its full localization due to the uncertainty
principle [2, 3, 42].

Wavelets are a class of functions, comprising an ensemble with hundreds of different
functions. Two of the most common wavelets are Haar wavelet and Morlet wavelet, which
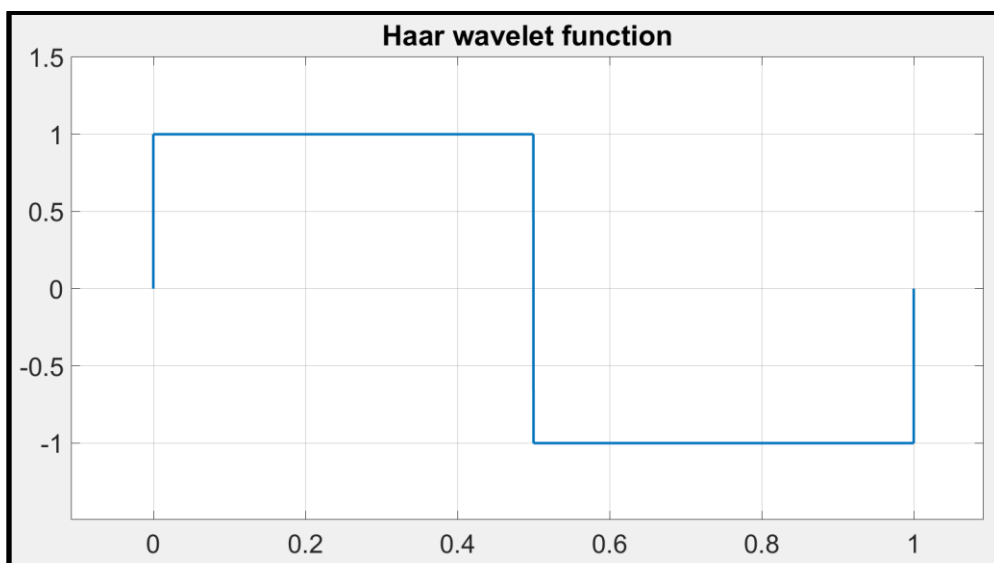are shown in Fig. 3.2.1 and Fig. 3.2.2.

Fig. 3.2.1 – The Haar wavelet, one of the first wavelet functions. Figure generated using
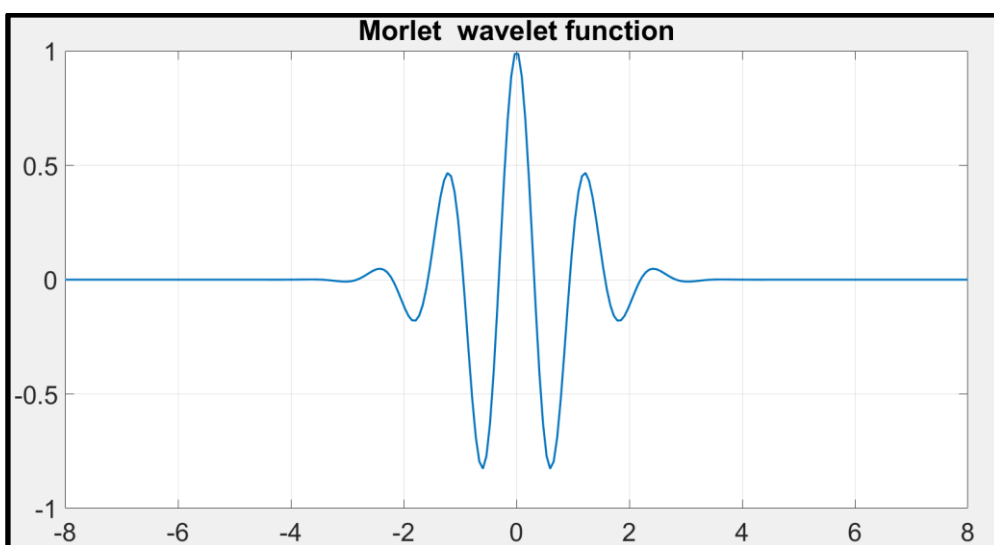MATLAB.

Fig. 3.2.2 – The Morlet wavelet, a very common wavelet function. Figure generated using MATLAB.

As a class of functions, there are two requirements that wavelets need to fulfill: admissibility and regularity. Admissibility requires that a wavelet presents a band-pass spectrum, i.e., the wavelet must be oscillatory. Regularity states that the wavelet must be smooth and concentrated in both time and frequency domains [42].

Similarly to Fourier transforms, that express a function as a collection of sines and cosines, one can express a function in terms of wavelets. The process is known as Wavelet Transform.

3.2.1 Wavelet Transform

The Wavelet transform consists basically in analyzing an incoming signal in terms of shifted and scaled versions of a basis function. This basis function will be one of the different types of available Wavelet functions, and will be referred as mother wavelet $\Psi(t)$. The shifted and scaled versions of the mother wavelet are parametrized by the variables s and τ. These altered versions will be represented as [4, 42]:

$$\Psi_{s,\tau}(t) = \frac{1}{\sqrt{s}} \Psi\left(\frac{t-\tau}{s}\right) \quad . \tag{38}$$

Note that the wavelet function Ψ is not specified, since the user is free to choose which wavelet to use. The factor $1/\sqrt{s}$ normalizes function amplitude across different scales. The variable s is responsible for scaling the mother wavelet, while the variable τ works translating the basis function along time or space. The scale property determines the extent of stretching or compression applied to a wavelet. A fundamental relation that needs to be mentioned is that the spatial (or temporal) scale, which in this case is connected to the frequency of the wavelet. The most compressed versions of the mother wavelet are usually able to extract the higher frequencies of the original function [4, 42]. Intuitively, the most stretched versions of the mother wavelet will then extract low-frequency information from

the signal. The visual consequence to the wavelet of varying this parameter is shown in Fig. 3.2.3, in the upper panels.

The parameter τ is responsible for situating the mother wavelet, usually in time. In other words, this variable's function is used to shift the original wavelet to the left or to the right. This is the property mentioned previously that mainly set apart wavelets from common sinusoidal functions. Their location is fundamental since wavelets are finite. This will make possible to study not just "which" frequencies are present in the signal, but also their distribution through time or space. The visual consequence of varying this parameter for a single wavelet of is shown in Fig. 3.2.3, in the lower panels.

Fig. 3.2.3 – Wavelets exhibits different layouts when scaled and shifted. In the upper panels, the original wavelet is positioned in the middle, flanked by its "stretched" and "squished" versions. In the lower panels, the original wavelet remains at the center, while its shifted versions are displayed. The wavelet used in this example is the Symlet4. The figure was made using MATLAB.

Qualitatively, the main idea of the wavelet transform is to analyze "how much" of a mother wavelet is in an incoming signal for a particular scale and location. This is done through the use of convolution. Convolution is a mathematical procedure performed on two functions to generate a third function. It describes the transformation of one function's shape influenced by the other. It is defined by:

$$(f * g) := \int_{-\infty}^{\infty} f(\tau)g\,(t-\tau)d\tau \quad . \tag{39}$$

The concept of convolution can be understood as an operation that returns the correlation between two functions. In other words, "how much" of function g is in f. This is exactly what is needed to proceed with wavelet analysis, justifying the use of this operation.

One of the first advantages of using wavelet decomposition arises already in the first steps. It is necessary to choose the mother wavelet that will be used in the process. There are hundreds if not thousands of wavelets to choose [2, 4, 42]. Since the whole operation is done convoluting the mother wavelet and the original signal, the similarity between them is an essential detail to be considered. The more similar the mother wavelet is to the signal, better the result of the decomposition is expected to be. This leaves the choice of wavelet free in order to match a signal.

After the choice is made, the wavelet of a particular shape and value of s is convoluted with the original signal while its location τ varies. This will return a coefficient:

$$c(s,\tau) = \int_{R} f(t)\,\Psi_{s,\tau}(t)dt, \quad s \in R^{+} - \{0\}, \quad \tau \in R \quad . \tag{40}$$

The process will be repeated for different values of scale, generating a set of coefficients. This coefficient $c(s,\tau)$ is known as the wavelet coefficient, and their quantity depends on the level of decomposition. Note that they depend on both scaling and shift parameters, consequently, the wavelet transform of a one-dimensional signal is a two-dimensional coefficient. In the following sections the usage of wavelet to analyze images will be depicted. Although possible (and very useful), it is a complex mathematical task since the wavelet transform of a two-dimensional signal (an image) generates a four-dimensional coefficient which is extremely complex to visualize. Gladly this problem is attenuated by one of the properties previously mentioned, regularity. This requirement secures fast amplitude decrease with decreasing scale [4, 42].

Another crucial property that makes wavelet transform as well as Fourier transform useful is the reversibility. Without the ability to return from the frequency domain, these transformations would not be nearly as powerful as they are. It is possible to transit to the

frequency domain, extract meaningful data and return to the original signal. To synthetize the original signal from the wavelet coefficient one proceeds as follows [42]:

$$f(t) = \int_{R+} \int_R c(s, \tau) \, \Psi_{s,\tau}(t) ds \, d\tau, \quad . \tag{41}$$

Just like in Fourier transform, wavelet transform can be implemented in continuous and discrete methods. The continuous wavelet transform employs every possible wavelet across a spectrum of scales and locations. This would result in an infinite number of scaled versions of the mother wavelet, convoluted with the original signal at infinite different locations, which is impossible to digitally compute. The discrete wavelet transform in other hand uses a finite set of scaled mother wavelets convoluted at finite number of locations. This comparison is analogous to the discussion carried out on continuous and discrete Fourier transform. As computers deal with discrete signals it is much more convenient to use the discrete wavelet transform in the scenario of digital signal processing.

3.2.2 Discrete Wavelet Transform

The discrete wavelet transform works as follows. A one-dimensional discrete signal is the input, that will be decomposed into wavelet coefficients. The first decomposition generates two level 1 coefficients, approximate coefficients cA_1 and detail coefficients cD_1. To obtain these coefficients the original vector is convoluted with a low-pass filter and with a high-pass filter, followed by dyadic decimation. Dyadic decimation or down-sampling, in signal processing, refers to the process of reducing the number of samples in a signal by removing some of the samples while retaining the essential information. This process keeps only the even elements in the vector. These filters are essentially the altered versions of the mother wavelet. The low-pass filter originates the approximation coefficient cA_1 and the high-pass filter originates the detail coefficients cD_1. This process is done recursively to obtain the approximation and detailed coefficients at next levels [42]. A diagram of the procedure can be seen in Fig. 3.2.4.
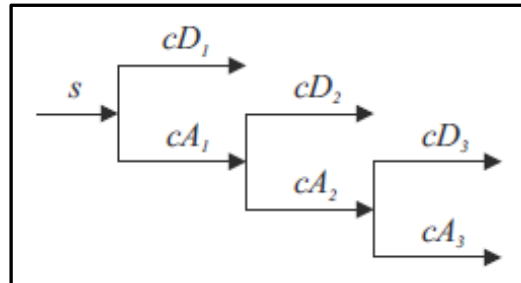
Fig. 3.2.4 – Qualitative illustration of discrete wavelet transform of a signal **s** at level three. Figure taken from reference [42].

The discrete wavelet transform is then capable of evince tenuous but relevant details of digital signals. However, just decomposing a signal in its wavelet terms achieves no significant result at all. The decomposition shows trait that other techniques can take advantage of. Together with thresholding, for example, the wavelet transform can be used to extract unwanted noise from a variety of signals [10-12]. Through threshold, some values of the details coefficients that are related to common noise are suppressed. Since these details are small, their suppression barely affects the main features of the signal [2]. That is, in a simplified and qualitative manner, how wavelet denoising works. This subject will be further explained in the following subchapter.

The term thresholding refers to a common technique in signal processing used to separate relevant information from noise or unwanted components. It consists basically of setting a threshold and classifying the data based on whether their values are above or below that threshold. There are different thresholding types depending on what is done to the classified data. Usually, their value will be set to be zero if below the threshold, and remain unaltered if above. This is the most common thresholding process, known as hard thresholding. Nevertheless, the determination a threshold value is not trivial. There are several different thresholding methods in signal processing. It is worth mentioning that there are automatic thresholding determination methods, that obtain threshold values in function of the input signal. One of these methods is the fixed-form threshold, that is proportional to $\sqrt{log(length(x))}$, being x any data vector.

As signal processing is necessary for almost all areas that carry out studies with measurements and data, it is expected to observe the use of wavelet transform for a wide range of fields. Applications range from medical electrocardiograms [6] to FBI fingerprint storage [8]. Together with thresholding, wavelet decomposition excels in roles such as compressing, sharpening, enhancing and denoising images [5, 7, 9-12]. This led, for example, to the usage of this technique in tomography [26] and to denoise ultrasound [10] images.

Wavelets also have remarkable roles in SPM image processing [22, 23]. In the last decades wavelets have been vastly used in pair with AFM. Among a plethora of usages, some worth mentioning are the analysis of thin film images, development of a fast-imaging method with self-tuning scanning frequency, the study of force-extension curves and denoising [13-19, 25, 27, 28].

Wavelets are also used in lesser extent to few STM applications. One of the various details that the frequency domain make explicit are the edges of an image. This happens because the pixel intensity value changes drastically in the edge, corresponding to a very high spatial frequency at that location. Taking advantage of this, wavelet decomposition was used to track atoms in STM-made movies [20]. Wavelets were also used to segmentate STM images [21] and remove artifacts and noise through sparse coding [29].

3.2.3 Practical Implementation

As already mentioned, the implementation of the discrete wavelet transform is done using MATLAB. MATLAB is a programming platform that consists in a matrix-based language. This platform was chosen because, in addition to being able to process data, it is also possible to develop complex algorithms. These algorithms can not only automate procedures to large datasets, but also be used to implement specific data treatments tools that are not feasible in other common data processing tools. Additionally, STM data is usually stored in matrix format, favoring the use of MATLAB.

The practical procedure of wavelet denoising is, in a simplified manner, divided in three parts. Decomposing the original signal in wavelet terms, determining the threshold values and setting to zero values below the module of the threshold for the detail wavelet coefficients. Suppose a file in a xy format with two columns, one for positions and the other

for height. This signal is stored in a matrix variable in MATLAB. The discrete wavelet decomposition is made through the command "*wavedec*". This command receives the initial signal *s*, the level of the decomposition and the name of the desired mother wavelet as input. As output the command returns the detailed and approximation coefficients, respectively *d1* and *a1*. As a first example, an x-ray diffractogram is used and decomposed in Fig. 3.2.5 at level one wavelet coefficients. The initial signal *s* is decomposed in the approximation coefficient *a1* and detail coefficient *d1* using the wavelet Symlet4.
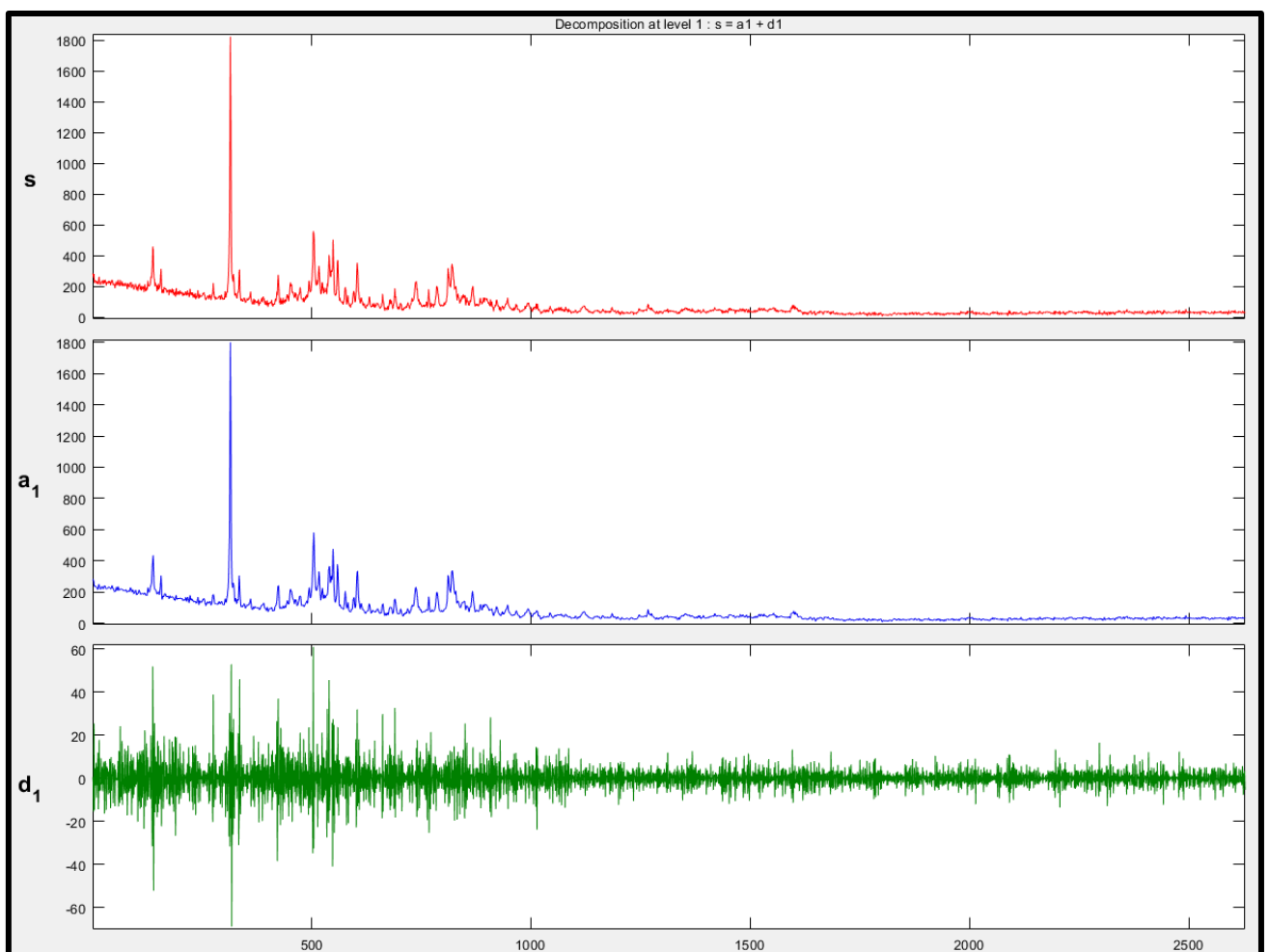

Fig. 3.2.5 – The discrete wavelet transform of an arbitrary x-ray diffractogram at level one decomposition.

In a deeper decomposition, the next step is to decompose the approximation coefficient *a1* into a second level detail and approximation coefficient, *d2* and *a2*, for the level two decomposition. The process continues analogously for further levels, as show in

Fig. 3.2.4. It is important to note that the decomposition level and the mother wavelet can be easily chosen and switched to observe different results. This facility is very useful for choosing the best mother wavelet and best level of the decomposition through trial and error.

For the denoise operation one of the thresholding determining functions is used. For example, the function "*wthrmngr*" in MATLAB is used with inputs of the determining function and the wavelet coefficients. The output returns the estimated values of threshold for the specific signal. The ease of carrying out this process is remarkable since the user can try different methods to discover which one better suit his/her problem.

For the last part, the detail coefficient will have values that are below the threshold set to zero (for the case of hard threshold). The last function used is "*cmddenoise*", which receives as input the original signal, the mother wavelet, the level of the decomposition, the estimated threshold value and the type of threshold done (soft, hard, etc). The output is the denoised signal. In MATLAB, besides the automatic threshold estimation, the value can be changed manually. The threshold value is represented by the blue dashed line in Fig. 3.2.6., and it can be dragged up and down.

Therefore, these three functions ("*wavedec*", "*wthrmngr*" and "*cmddenoise*") are used to perform a satisfactory wavelet decomposition and denoising in a one-dimensional signal. The two-dimensional case is obtained analogously, with analogous MATLAB functions.

The result of the denoising process will be omitted, since only an explanatory example is provided in this section and the level one denoising does not significantly changes the result. In the selected diffractogram most of the noise in a signal is found in the further levels of detail wavelet coefficients.

Now equipped with STM and signal processing theory, it is possible to depict and discuss the results obtained during the study of discrete wavelet transform to denoise and enhance spectroscopic contrast in STM images of Cerium Oxide.
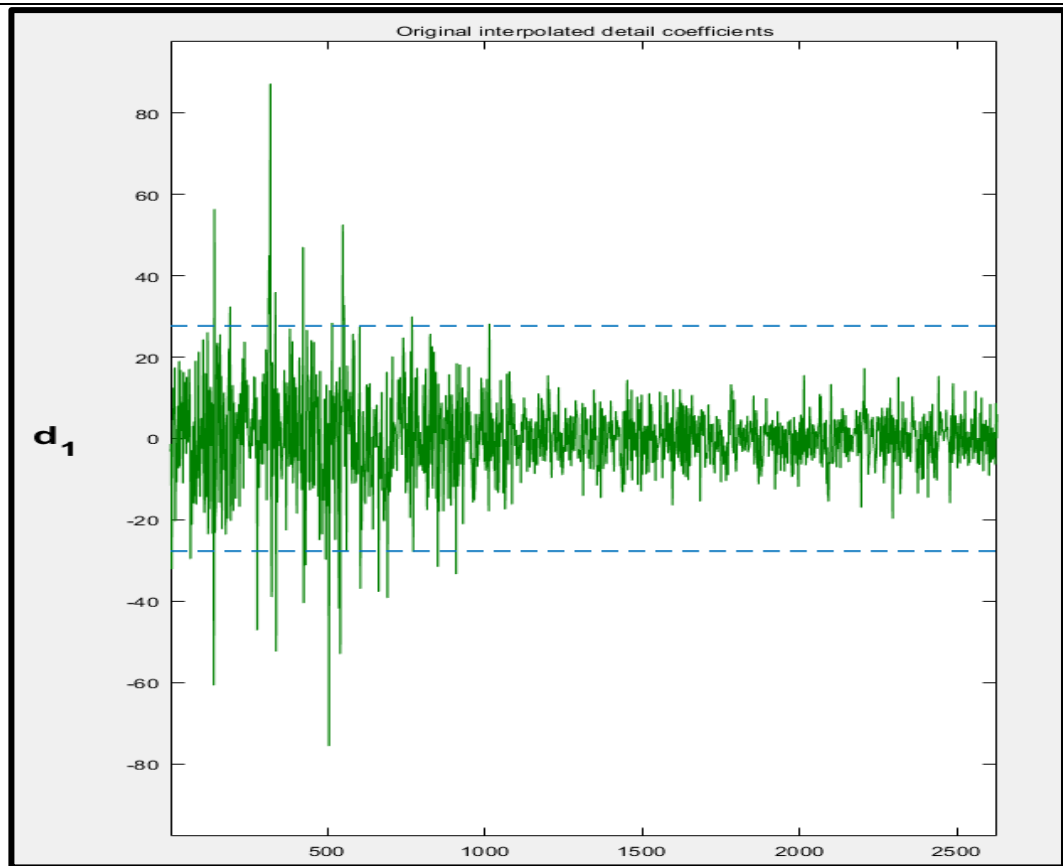
Fig 3.2.6 – Application of the threshold procedure. The blue dashed line represents the threshold value estimated. All values below the module of the threshold will be set do zero in the detail coefficient vector data.

4. RESULTS

Before going to the results, it is important to discuss about the electronic properties of the sample, as well as the growth method.

4.1 Cerium Oxide Properties

The intrinsic reduced energetic cost for reduction or oxidation of cerium oxide (CeO_2) allows the use of this compound to control the release or absorption of oxygen depending on the environment that surrounds it. For this reason, CeO_2 is conventionally used for combustible or toxic gas sensors and as a catalyst for oxidation reactions of CO and CH_4. The crystalline orientation of the exposed facets and the morphology of ceria nanoparticles (NPs) affect their catalytic and sensing capacity, so NPs with different shapes such as nanorods, nanocubes, planar clusters, among others, have been synthesized to improve the efficiency of the catalyst [51]. Doping possibilities have also been shown as an interesting route for the generation of active defects such as oxygen vacancies, which play an important role in the ionic conductivity of this material. Such property is desirable for use as a solid electrolyte in fuel cells, as can be seen, e.g., in reference [52]. In addition, the selected dopants can also be selected among redox species, which provides an improvement in the catalytic activity [53].

In the same direction, the synthesis of this oxide associated with others systems such as metallic materials, nano-scaled carbon forms, among others, modifies its interaction with the environment, improving its chemical sensitivity and/or catalytic properties [50, 54, 55]. On the other hand, graphene sheets have been successfully used for anchoring metallic oxide NPs aiming the stabilization of their morphology as well as tuning their redox properties and enhancing conductive (electrical) properties of ceria [56, 57]. These different studies have shown the relevance of the surface of CeO_2, as well as its interactions when associated to other materials. Therefore, it is evident that a two-dimensional configuration could significantly improve both aspects. Despite the promising results presented in the literature in relation to the catalytic and chemical sensitivity of the CeO_2-nanocarbon system, so far there is no study aimed at understanding in more detail the mechanisms of

interaction and alternatives for its improvement and manufacture in a more controlled manner.

A detailed study of the growth parameters of ultrafine nanostructures of ceria (pure and doper) on graphene, to tune ceria properties such as shape, crystallographic orientation, concentration of vacancies and prevalence of Ce^{3+}, analyzing its consequences on electric conductivity characteristics is still missing. In order to improve these properties, materials used as CeO_2 dopants must produce defects in the ceria structure, such as oxygen vacancies and Ce^{3+}, which will increase the ionic and electronic conductivity, respectively. Such conditions will allow the use of the CeO_2/graphene system both for catalytic applications and as a sensor for gases such as CO and NO_2 [58, 59].

4.1.1 Ultrafine CeO$_2$ growth in HOPG substrate

The Pulsating Laser Deposition (PLD) technique allows a broad range of applications on growth of films using different classes of materials with the advantage of keeping the stoichiometry of the used targets. This allows a simple route for deposition of complex films [60, 61]. The method basically consists on the evaporation of a target material that is deposited through the surface heating produced by a pulsed high energy laser. The evaporated material is ejected as a plasma that moves along a plume-shaped path directed towards the desired substrates, later forming thin films. Parameters such as laser wavelength, substrate temperature, pulse frequency, oxygen partial pressure during deposition, fluence, target distance and deposition time can be tuned to modify the stoichiometry, morphology, orientation and crystalline quality of the deposited films.
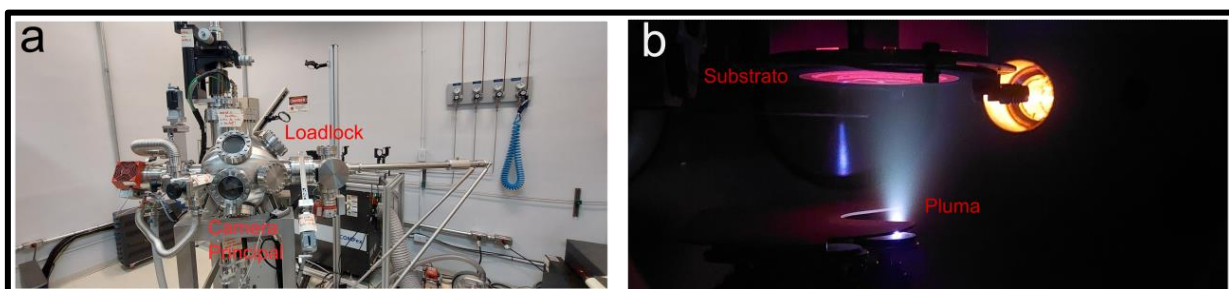

Fig. 4.1.1 – PLD Reactor. a) External part of the reactor. In the red text can be read "Loadlock" and "Main Chamber". b) Main chamber interior. In the red text can be read

"Substrate" and "Plume". The photographs were provided by Diego Lopes, a collaborator responsible for sample growth at UFABC.

The reactor used for the growth of ultrafine ceria films studied in this chapter was developed by the Dutch company TSST (Fig. 4.1.1) and consists of a pulsed laser with a wavelength of 248 nanometers, a deposition camera with carousel for five different targets and a gas entrance for deposition in an oxygen-controlled environment. Both the exchange of targets and the loading of samples is carried out through a load lock chamber located on the side of the main camera, allowing to maintain a constant high vacuum in the main (growth) chamber (Figure 4.1.1).

Initial deposition tests were performed on graphene and HOPG substrates simultaneously, in order to verify morphological differences of the grown nanostructures as a function of the surface energy of the sp^2 carbon substrate.

Cerium Oxide has the fluorite structure (space group Fm3m). It is a face-centered cubic (FCC) structure that is common for compounds with the formula AB_2, where the A ions occupy the eight tetrahedral interstitial sites whereas B ions occupy the regular face-centered cubic sites. The main structure of CeO_2 is shown in Fig. 4.1.2.
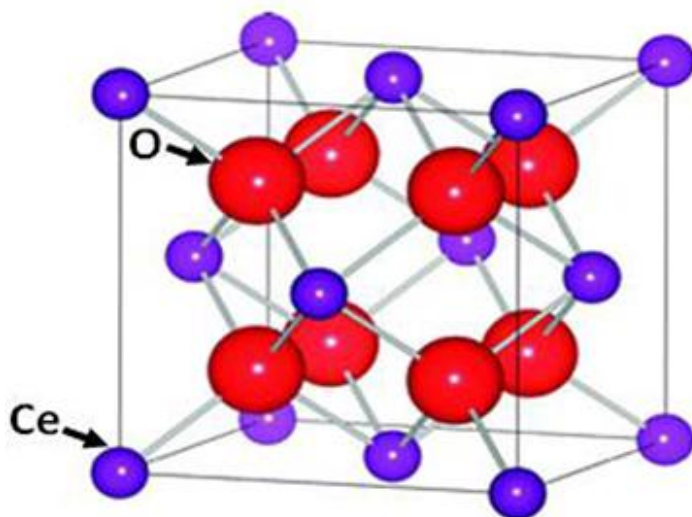

Fig. 4.1.2 – Schematic representation of the cubic fluorite structure of Cerium Oxide. Figure taken from reference [66].

It is known in literature that CeO_2 has a lattice parameter of 0.54 nanometers [63]. To characterize and validate the sample, measurements were conducted at a nanometric scale using the STM. The images obtained are of fundamental importance, since the ability to visualize the atomic structure allows the experimental verification of the lattice parameter of CeO_2, as well as a confirmation of its structure and observation of its orientation. The atomic structure of CeO_2 obtained can be seen in Fig. 4.1.3.
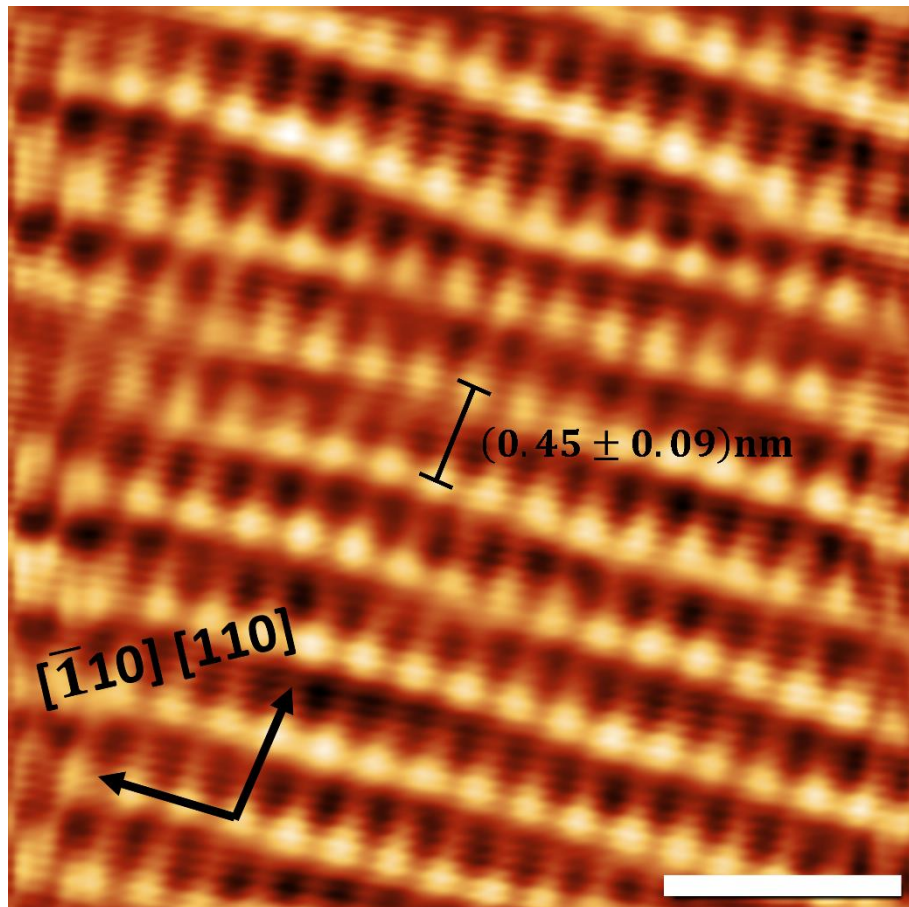

Fig. 4.1.3 – Atomic resolved STM image of CeO_2 in HOPG substrate. The scale bar is 1 nanometer.

A height profile was extracted from the results of Fig. 4.1.3 along the direction [110]. As expected, due to the oscillating pattern, the profile was similar to a sinusoidal graph, with the peaks corresponding to the white dots in Fig. 4.1.3. To achieve a reliable experimental estimation of the lattice parameter, the average difference between multiple peaks was taken into consideration. The error was determined by calculating the average width at 3/4 height across multiple peaks. The (110) interplanar distance obtained $(0.45 \pm 0.09)nm$

agrees with the observed in literature (0.38 nm) within the error bar. The CeO₂ orientation seen in Fig. 4.1.3 is expected, as seen in reference [65].

Another relevant CeO₂ characteristic is its characteristic band structure. From the theoretical calculations it is possible to obtain an estimation of the band gap, intrinsically related to its density of states (DOS). This allows a comparison of STS measurements with the predicted band gap, providing an additional confirmation of the sample's stoichiometry and structure. From Fig. 4.1.4 it is possible to observe CeO₂ has an indirect gap of approximately 1.86 electron-volt [64].
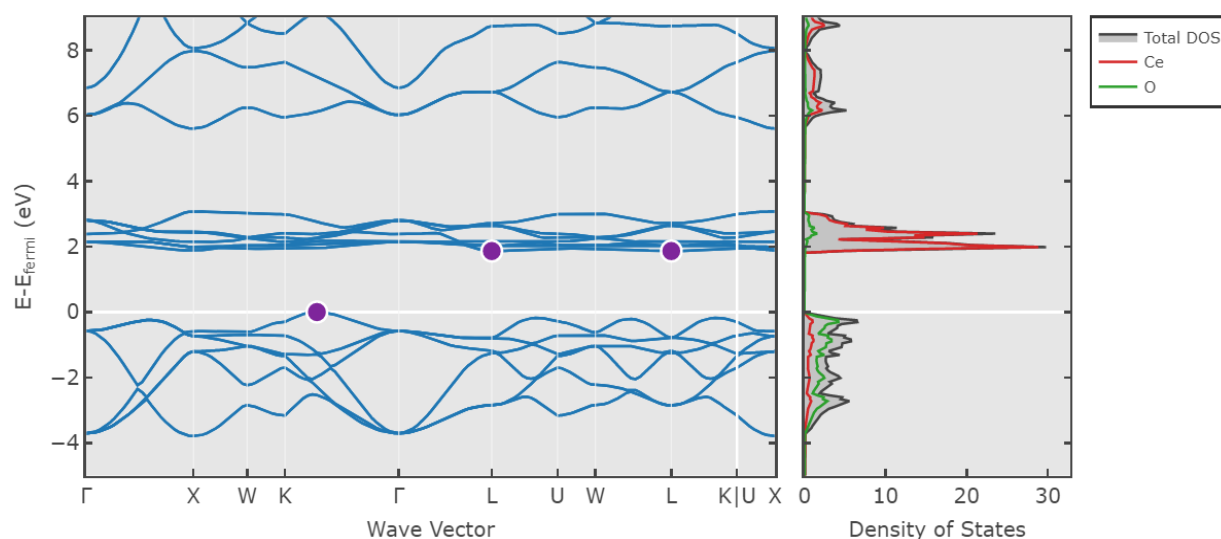

Fig 4.1.4 - CeO₂ band structure and Density of states. Figure taken from Materials Project website.

Several STS measurements were carried out at the exposed HOPG substrate and the grown CeO₂ clusters and nanoparticles. The results are shown in Fig. 4.1.5. The methodology for acquiring the STS curves involved capturing a high-quality STM image in the border of the substrate and CeO2 interface. Subsequently, multiple STS curves were collected from both surface terminations. The average of the curves is calculated to yield a more accurate representation, eliminating possible surface artifacts. As anticipated for HOPG, the substrate exhibits a semimetal curve, while STS measurements in CeO₂ depicts a semiconductor curve with an estimated energy gap of approximately 1.87 electron-volts.
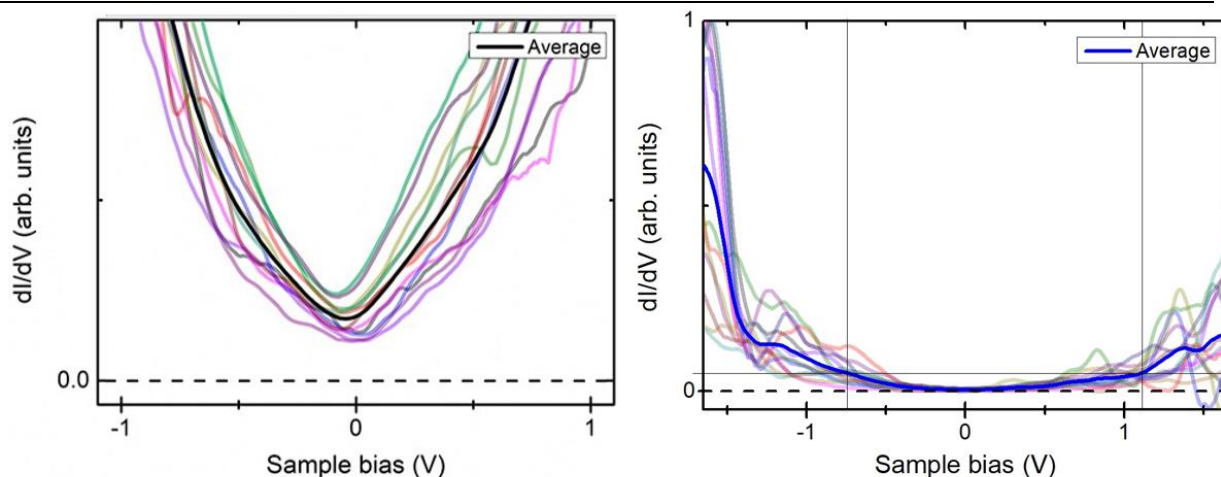
Fig. 4.1.5 – STS measurements in HOPG (left panel) and CeO$_2$ (right panel).

4.2 Calibration Method

The main goal of this work revolves around using wavelet transform to de-noise STM images at distinct applied bias, providing reliable datasets in which spectroscopic information can be qualitatively disentangled from sample topography. For this to be done correctly and efficiently it is convenient to validate the method testing it with different parameters and in different image datasets. It is also mandatory to define procedures to evaluate the results after de-noise is carried out. To make sure the method is functional to SPM images (including AFM data), an analysis in four main steps is suggested here. The first step consists in analyzing visually the image before and after de-noises, eliminating coarse results right away. After that, in the second step, topographic profiles are extracted from pre-processing images and post-processing images. These profiles answer important questions such as if the process keeps the height and volume under the curve of primary peaks, if the method strongly smooths smaller peaks or grain borders, etc. The third step is to obtain a Fourier Transform of the two profiles to observe what happened in the frequency domain before and after the application of the method. Last but not least, a residual image obtained by subtracting the original image and the treated image is generated. The residue indicates the amount of original information suppressed from the image. In order to explain all these steps, we use two test images, one from STM and one from AFM. Such method calibration will be depicted in this section.

The test images are shown in Fig. 4.2.1. The first image (Fig. 4.2.1 a) is an AFM measurement of Bi_2Te_3 sample in HOPG substrate. The second image (Fig. 4.2.1 b) is a STM measurement of bilayer graphene in silicon substrate. These images were obtained from the STM and AFM software, exported as a xyz file. Such file type is easily handled by MATLAB, that fully access the three columns (2 for plane positions and the third for height), making possible to reconstruct the image through the use of the command "mat2gray". The process outlined here performs the de-noise procedure in both images with several different mother wavelets, in various decomposition levels. This initial stage indicates the most suitable wavelets to use in SPM images. The choosing method consists of trial and error, but with good candidates suggested by reference [10]. Some of the mother wavelet tested are Haar, Daubechies, Symlet, Biorthogonal and Discrete Meyer. It is relevant to state that the wavelets mentioned are in reality families of numerous functions.
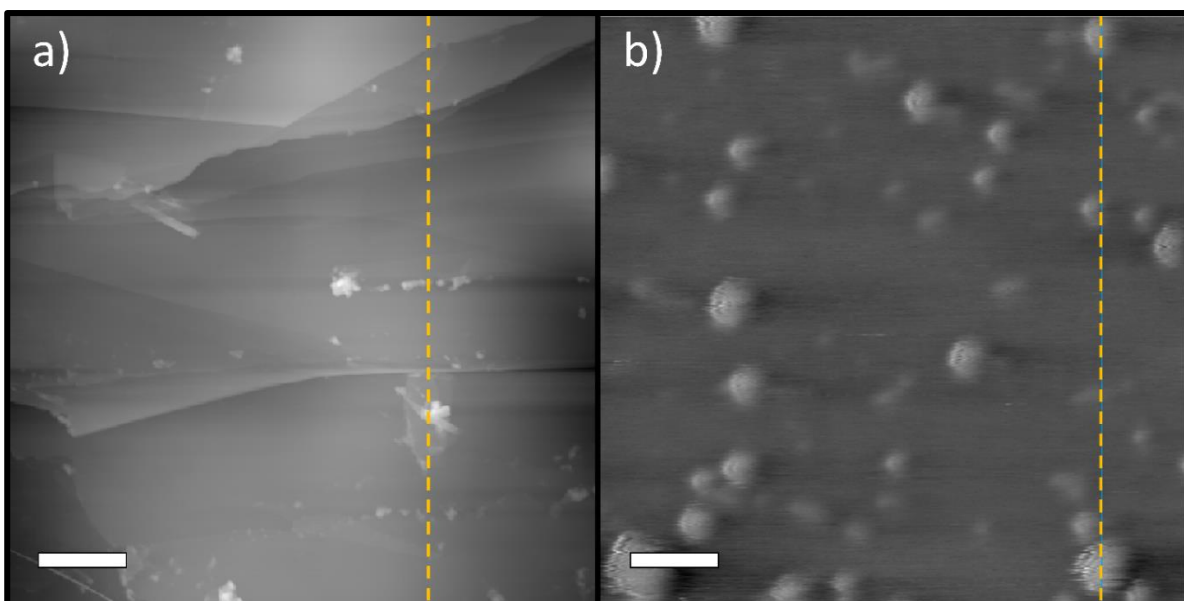

Fig. 4.2.1 – a) AFM image taken from a Bi_2Te_3 sample. The lateral scalebar is 1µm and the height ranges from 0 to 30nm. b) STM image taken from a bilayer graphene sample. The lateral scalebar is 100nm and the height ranges approximately from -0.1nm to 2nm. A vertical profile is extracted along the yellow dotted line in both images.

The majority of the wavelets tested resulted in identical images before and after the denoising processing, meaning that no relevant gain was obtained using the method. In the other cases, the processing method caused the processed image to become distorted, i.e.,

relevant data was being incorrectly suppressed from the original image. For this extreme cases it is easy to determine which mother wavelets should not be used for this specific study, just by looking at the processed images. It is expected to obtain a cleaner image, with less artifacts in the background. To exemplify this, a discarded parametrization can be seen in Fig. 4.2.2, where the image become pixelated and distorted.
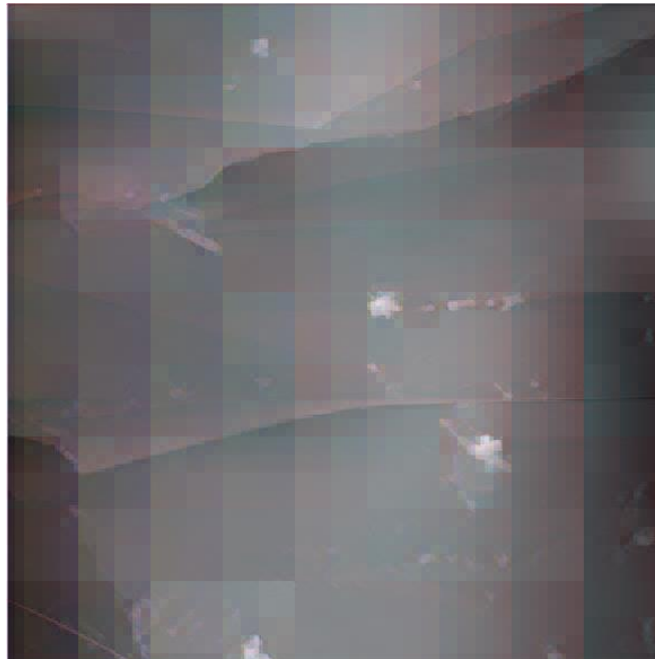

Fig 4.2.2 – A discarded processed version of the Fig. 4.2.1.

The first step of the calibration method is completed then just by elimination of two types of results, the strongly modified ones, and the fully unmodified ones. That classification led to the good candidates, in our case some different wavelets from Symlet family and from Biorthogonal family. Although we have tried to de-noise using distinct functions, the Symlet wavelet was expected to be among the best choices, since it has been used in similar works [10]. The Symlet family consists of infinite modified versions of Daubechies wavelets, that starts with one and grow, with small modifications. Symlets from two to eight have been tested showing small difference for small number and virtually no difference for greater numbers. The best mother wavelet for the two test images was the Symlet4 wavelet (Fig. 4.2.3), once again chosen by testing different functions and observing which function had the best result, i.e., trial and error. We believe the Symlet4 showed the best results due to the similarity of its form compared to most common form of noise in

topographic profiles in SPM. This similarity is related to better results due to the intrinsic convolution-dependency of this method, which has been already discussed in the previous chapter. Using this function as a mother wavelet allows then to effectively extract undesired noise.
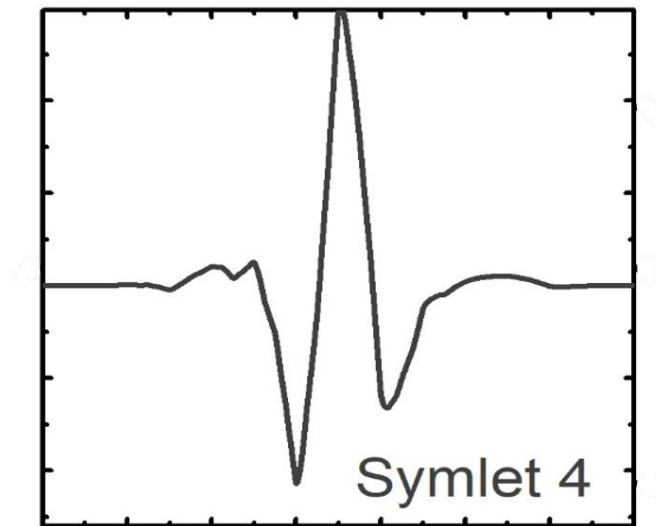

Fig. 4.2.3 – The Symlet 4. This wavelet was chosen as the main mother wavelet in this work through the method of trial and error.

An additional parameter that deserves particular investigation in initial tests with the method is the level of decomposition. This parameter is intrinsically related to the threshold value, which determines how much of the detail coefficient will be suppressed. Despite that, as the threshold value used in this work was determined automatically for each input image, it is convenient to assume the threshold as constant and focus the discussion in the decomposition level. Low decomposition levels lead to few or zero changes between the pre-processing and post-processing image. This means that with a few-level decomposition the relevant noise of SPM images remains untouched, requiring further levels of decomposition. As the level of decomposition increases to 4-5, it is possible to extract noise satisfactorily. However, as the level of decomposition increases beyond level 6, the result becomes artificial. This happens since at higher levels more detail coefficients are extract from the data and relevant features end up being inadequately suppressed. For the majority of tests, a level of decomposition between 4 and 5 has proved to be sufficient for our purpose. Fig. 4.2.4 is an example of a visually satisfactory denoising process for the first step.

This result was obtained using suitable parameters as discussed above. It is shown that the right image in Fig. 4.2.4 has reduced static noise and smoother profiles, characterizing noise reduction but with reduced loss of information in edge details.
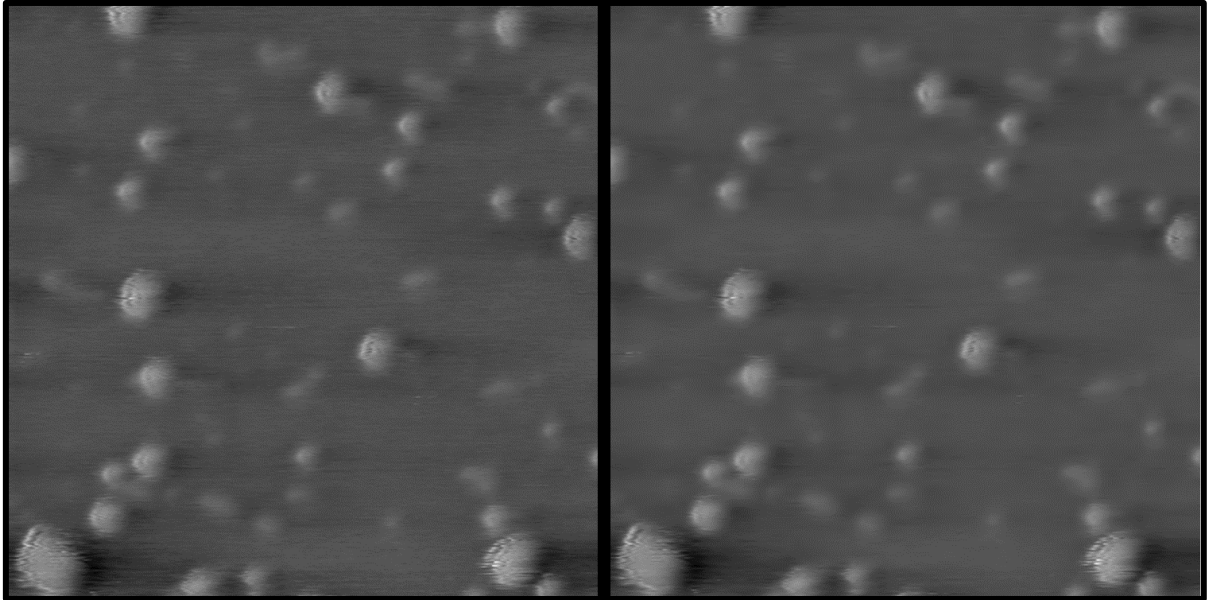

Fig. 4.2.4 – Visual result of the wavelet denoising processing a STM image of a bilayer graphene sample. The left image is before the treatment and the right image is after the treatment. The decomposition was performed using Symlet4 at level 5, with soft thresholding.

After choosing a mother wavelet and a reference value for the decomposition level parameter, it is necessary to evaluate the denoise result in depth. To better visualize the difference between the pre-processed image and the post-processed image we extracted a vertical profile from both images, indicated by the yellow dotted lines in both panels of Fig. 4.2.1. The profile is preferably extracted in a vertical line if the horizontal line is the fast axis in the STM and AFM, which often results in scanning artifacts along horizontal lines. Both profiles are then placed side by side in order to allow visual analysis.

The extraction is carried out with MATLAB commands. Since the input (measurement) file provides access to each pixel in the figure. The extraction is usually performed simply by making an array with all pixels along a vertical line. It is also possible to read subsequent vertical lines and make an averaged profile using a limited range of horizontally distributed data. This process is performed before and after the denoise

procedure, generating two profiles for each image, one representing the pre-processing image and the other one representing the post-processing image. These profiles are shown in Fig. 4.2.5 and Fig. 4.2.6 for the Bi_2Te_3 sample profile and the bilayer graphene sample profile, respectively. In both cases, the blue line depicts the profile prior to denoising, while the red line represents the profile after denoising.
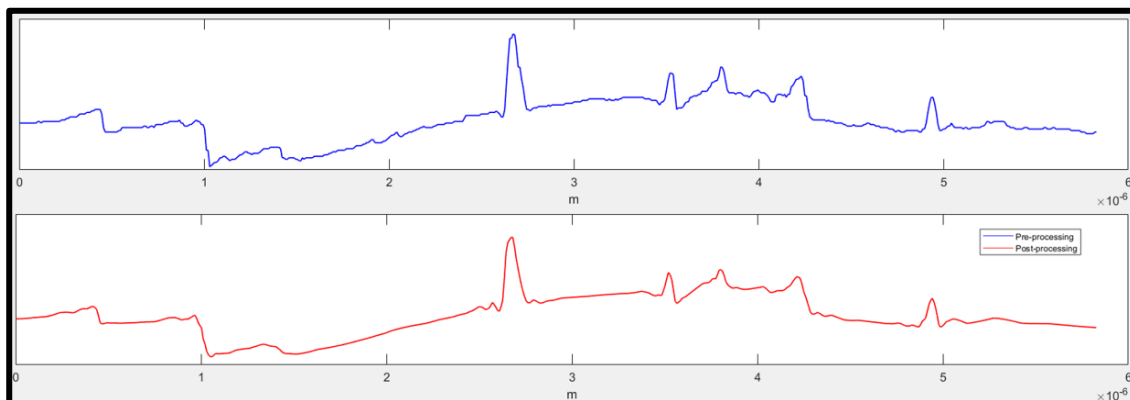

Fig. 4.2.5 – Topographic profile of Bi_2Te_3 on HOPG, extracted from the AFM image in Fig. 4.2.1. The profile was extracted along the yellow dotted line.
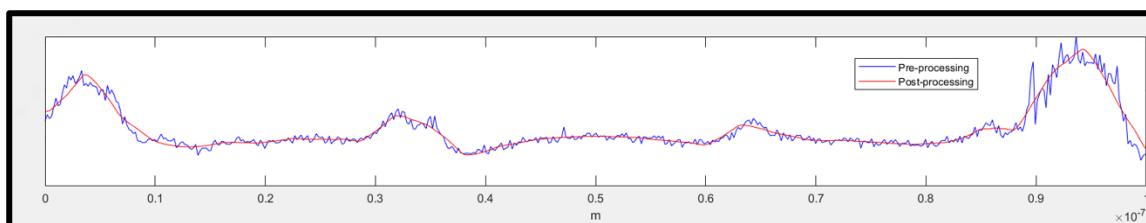

Fig. 4.2.6 – Topographic profile of bilayer graphene on silicon, extract from the STM image in Fig. 4.2.1. The profile was extracted along the yellow dotted line.

The visual analysis of the first profiles in Fig. 4.2.5 shows that the main shape of the profile remains unchanged. The most relevant peaks and valleys show little or no deformation, while the height and depth also remains virtually unaltered. The appearance of small peaks near the border of big peaks (in the vicinity of position 2.8µm in Fig. 4.2.5) is noted, which indicates that this method may introduce information near borders. This occurs due to the intrinsic tendency of wavelet transform denoise to smooth regions near steep borders. Some modification extent was already expected since no signal processing technique is perfect and this issue can be easily solved by applying the method to delimitate

regions of interest instead of processing the whole image. However, such changes are considered of minimum relevance for the scope of this work, and will not be addressed unless physical properties are modified. The low-amplitude aleatory oscillating pattern observed in the baseline of the figure prior to the procedure is attenuated. This pattern is commonly associated with multiple types of noise, either electronic, thermal (small variations in local temperature) or due to air convection. The overall profile clearly smooths after denoise when compared to its original version. This is a direct and unambiguous indication of noise removal.

In Fig. 4.2.6 it is possible to observe essentially the same effect discussed above. However, the difference between the profiles is substantial. This happens because the bilayer graphene image is, in general, a much noisier figure. This can be observed in Fig. 4.2.6 blue line, where the profile baseline exhibits very pronounced aleatory oscillations. This is expected since STM is carried out with a low current amplifier and a piezo scanner with a maximum 500nm scan range, rendering it much more sensitive technique compared to AFM. Therefore, STM images are more susceptible to larger noise contributions. The results in Fig. 4.2.6 are very interesting. The main peaks and valley are virtually unchanged, but with a significant difference in the base line of the profile. This difference is exactly what is observed in Fig. 4.2.4, where the static noise form in the background is largely suppressed over the whole profile. This strongly indicates that the method is relevant to denoise SPM images. However, it is observed that a possible double peak has been merged into one larger peak (around 33nm x-axis position). Therefore, it is important to state that the method has its limitations, given the appearance of incorrect data in small details and some degree of loss of relevant information near edges.

The profile visual analysis shows that the method is interesting for AFM images, and very promising for noise reduction in STM images. This concludes the second step of the four-step proposed to validate it.

Despite the choice of using wavelets, Fourier Transform is still a very powerful tool for frequency analysis in signal processing, so it is used to further evaluate the process. The third step consist in analyze the frequency spectrum of both profiles. It is expected to observe a suppression of all frequencies presented in the image, indicating a white noise (aleatory noise) removal. For this purpose, it is mandatory to use the Fourier Transform

discussed before (chapter 3) to transit from the spatial representation to the spatial-frequency representation. This is done simple by using the FFT command in MATLAB (Fast Fourier Transform algorithm). FFT is performed in the vector that stores the height information of the profile, i.e. the y-vector. However, the x vector (spatial variation along the line the profile was measured) needs to be re-scaled before FFT plotting to obtain the frequency histogram. The maximum possible frequency that can be observed is between two consecutive pixels, and the minimum frequency is between the first and the last pixel. After sampling the x-vector and plotting it with the y-vector we obtain the frequency histogram for both profiles, before and after the processing (Fig. 4.2.7).
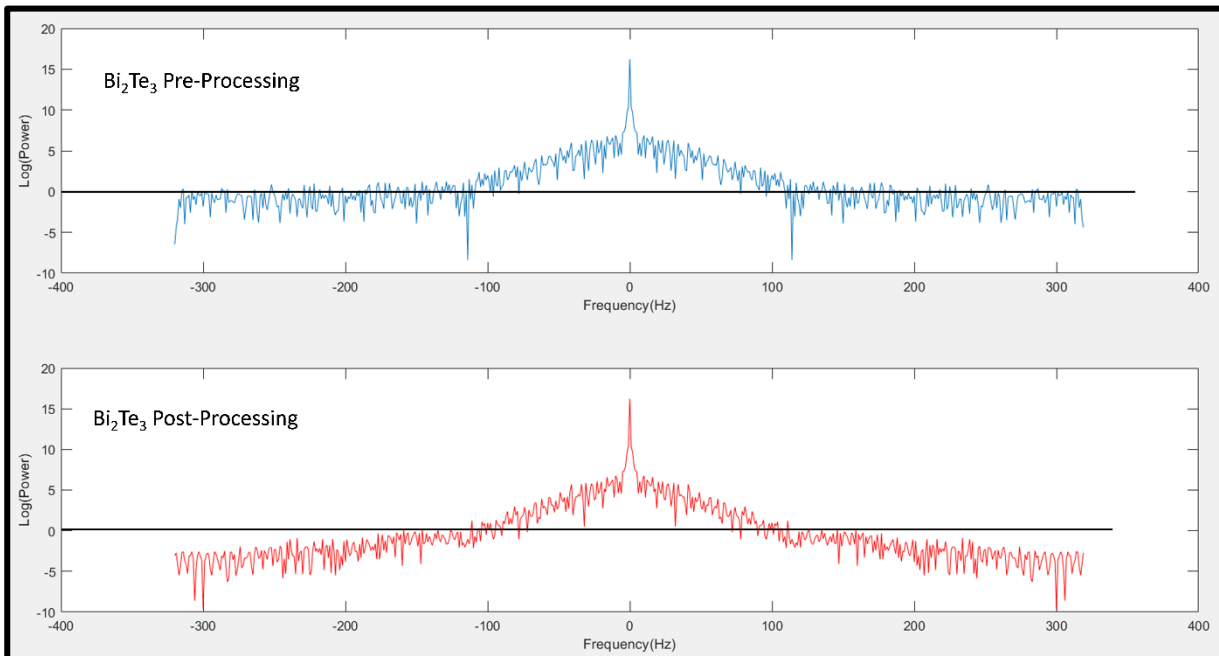

Fig. 4.2.7 – Frequency histogram obtained by FFT of the Bi_2Te_3 profile before (blue) and after (red) the denoising procedure. There is a horizontal line plotted in zero for reference.
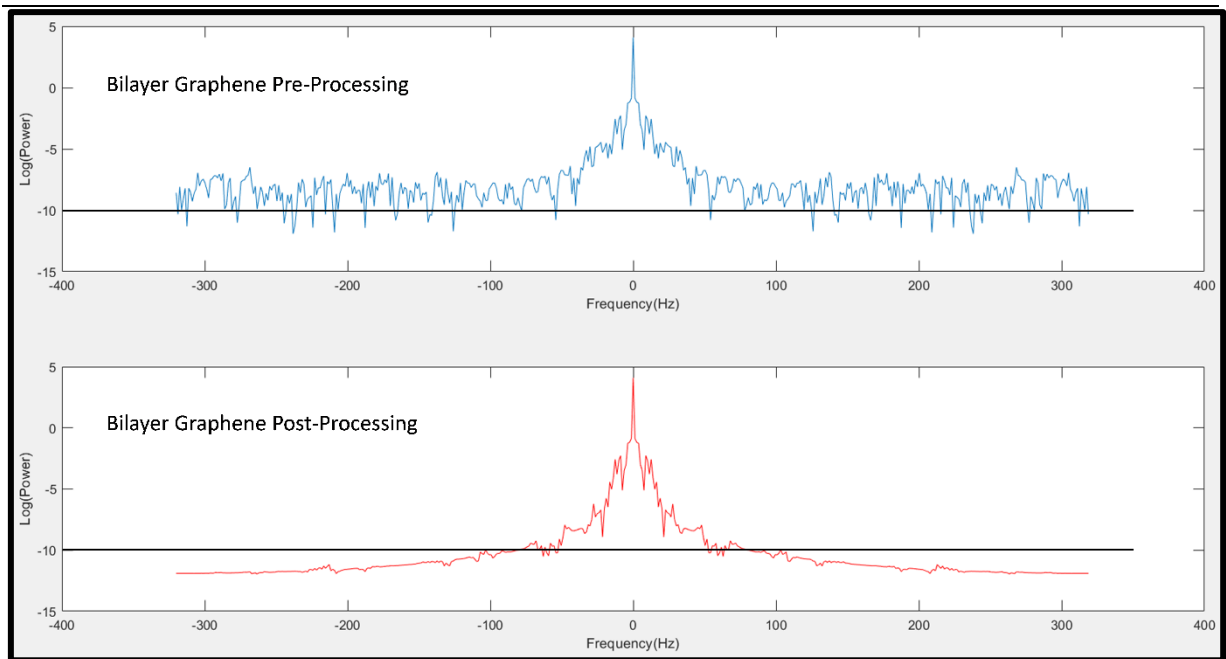
Fig 4.2.8 – Frequency histogram obtained by FFT of the bilayer graphene profile before (blue) and after (red) the denoising procedure. There is a horizontal line plotted in minus 10 for reference.

In figures 4.2.7 and 4.2.8 it is possible to observe a considerable reduction in the intensity for the whole spectra, which is associated with white noise removal. It is also noted a decrease in high frequencies, that possibly indicates the desired baseline noise reduction, and also the collateral edge smoothening. It is very interesting to notice a peak in a specific frequency in the blue profile in Fig. 4.2.7 around 110Hz. This reveals a concentration of data measured with a specific sampling frequency, which can be associated with a particular source of noise signal at a defined frequency in the image. The wavelet method was able to automatically extract that peak of frequency, without the use of common Fourier Transform tools in which one must select frequency peaks manually, as shown in the red profile in Fig. 4.2.7. Since there is minimum loss of relevant information after the treatment, it is safe to assume the peak is related to the presence of noise. Another indication of the successfulness of the method is the attenuation of the oscillating format, clearly observed in Fig. 4.2.8. This figure also exhibits a decrease in all frequencies, implying once again the white noise reduction. However, it is also observed the appearance of high frequency peaks around 300Hz in Fig. 4.2.7, that can possibly be related to the frequencies required to describe borders, as discussed previously (Fig. 4.2.5, approximately at 2.8μm). Nevertheless, the

results of the frequency analysis are consistent with expectations, presenting features that agree with those observed in previous steps. It is interesting to point out that the frequency histograms agree not only with the convenient part of the results, but also agrees with the issues observed in the previous steps.

For the last part of the wavelet procedure validation, a residual image of Fig. 4.2.4 is retrieved in MATLAB simply by subtracting the right and left image. The residue is of fundamental importance, as it is strictly related to the information removed from the image during the denoising process. Only the STM graphene bilayer image will be depicted in this last step since the noise reduction was more evident when compared to the AFM image. Figure 4.2.9 shows the residual image side by side with the original image.

The general information depicted in this residual image is that most of the information extracted from the original image is random, which indicates its relation to background noise. This is expected since the third step indicated a considerable remove of white noise of the image. Overall, the residual image also indicates a good result in the method. However, it is possible to observe in Fig. 4.2.9 that in fact there was some loss of information. This is indicated by the white circles drawn in the residual image, where there is a non-aleatory distribution (concentration) of information. Compared to the original image in the right, it becomes evident that this concentration is related to the presence of the nanostructures. Nevertheless, such reduced information loss from the method is acceptable when compared to the overall data quality gain observed in the previous steps.
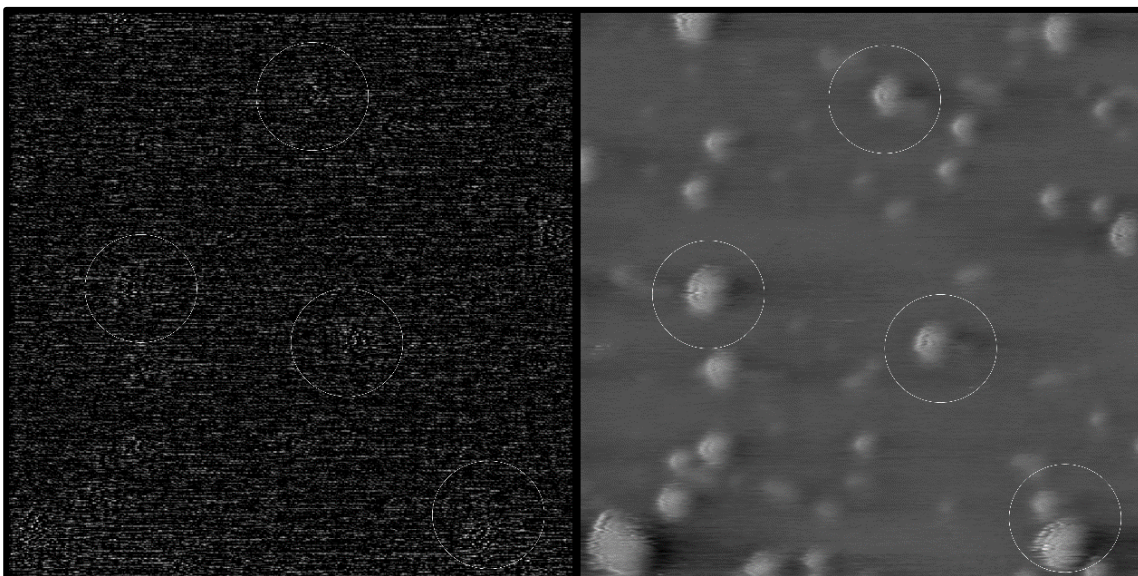
Fig. 4.2.9 – Residual image of Fig. 4.2.4 (left) and original image of bilayer graphene (right).

This concludes the four-step analysis, which is considered to be sufficient to validate the method, understanding and discussing its strengths and weaknesses. All steps indicate the method is reliable and can be used to improve the quality of SPM images, with emphasis on STM images. The improvement is crucial since it can be used to enhance weak contrast in the original image, evidencing physical relations that went unnoticed. Hence, supported by the method and aware of its reliability, we are able to proceed and apply it in Cerium Oxide STM measurements.

4.3 Image Series and Discussion

The main series of measures in this work are the CeO_2 thin films deposited in HOPG. In addition to Fig. 4.1.3 and Fig. 4.1.5, a set of the best measurements of CeO_2 at different applied bias (for the same current threshold) is depicted in Fig. 4.3.1. These images were generated in MATLAB using the xyz format file exported from the original measures in the STM software. While in the search for suitable images to utilize this method, we seek for samples with weak sample-substrate contrast, a situation that would render the contrast improvement more relevant. CeO_2 is exactly one of these samples, with weak contrast. Another desired feature, observed in CeO_2 sample, is that the image changes over tension variation. This is observed mainly because the STM image does not return a pure height response, as discussed in previous chapters. The measurement is a convolution between height and electronic states, therefore, changing the applied voltage in the system makes it sensitive to specific electronic properties of the sample, consequently generating different images.
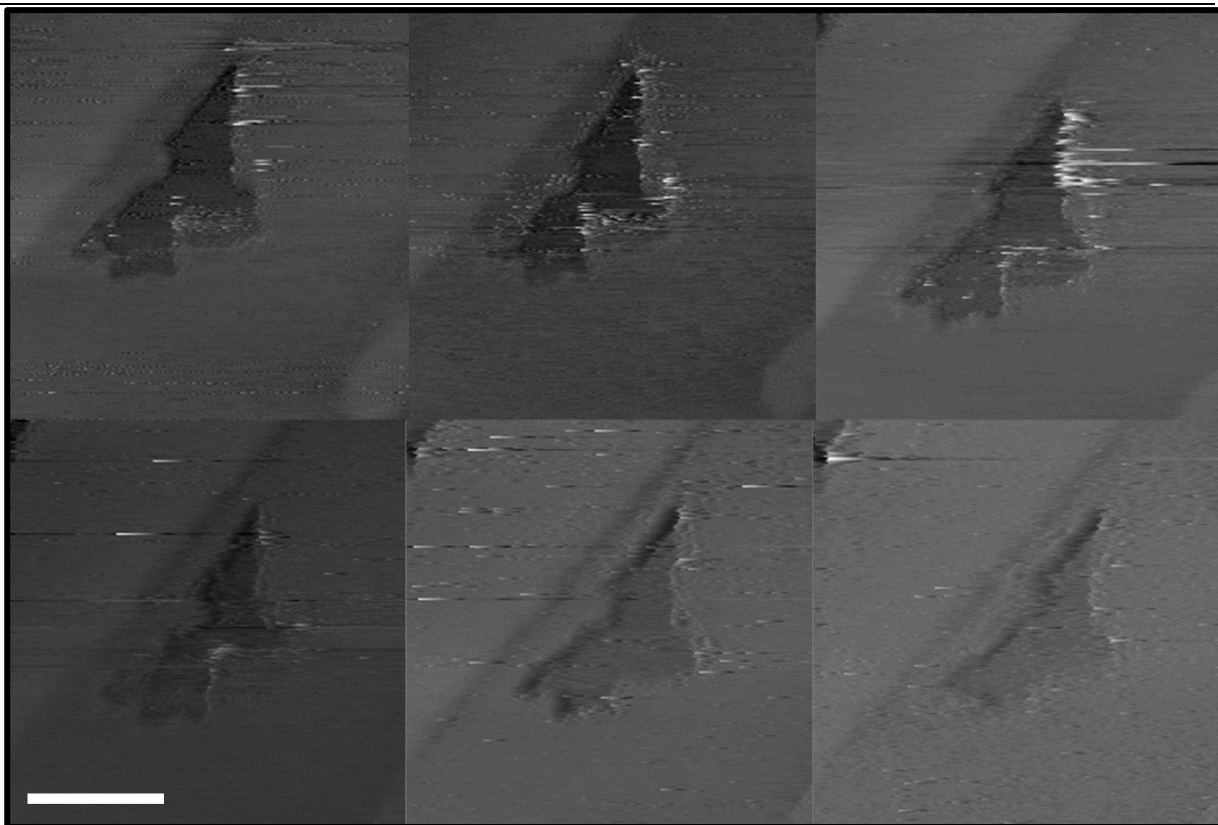
Fig. 4.3.1 – Series of CeO$_2$ nanostructures STM measurements in different applied bias. Respectively, 1V, 1.5V and 2V for the first row and 2.5V, 3V and 3.5V for the second row. All images share the same side length (54nmx54nm) and the scalebar is 20nm.

As the voltage increases, it is possible to observe a region disappearing and reappearing in the nanostructure. This can be clearer observed in Fig. 4.3.2 and points out to the existence of relevant electronic interactions around 2.5V. The main idea is not to propose the reason behind this phenomenon, but to state that the wavelet transform, together with denoising, can be used to enhance the weak contrast observed between the images in Fig. 4.3.2. In this case, the difference can be seen without further processing. However, there may be cases with other classes of samples in which such features would only be visible after image treatment with denoising.
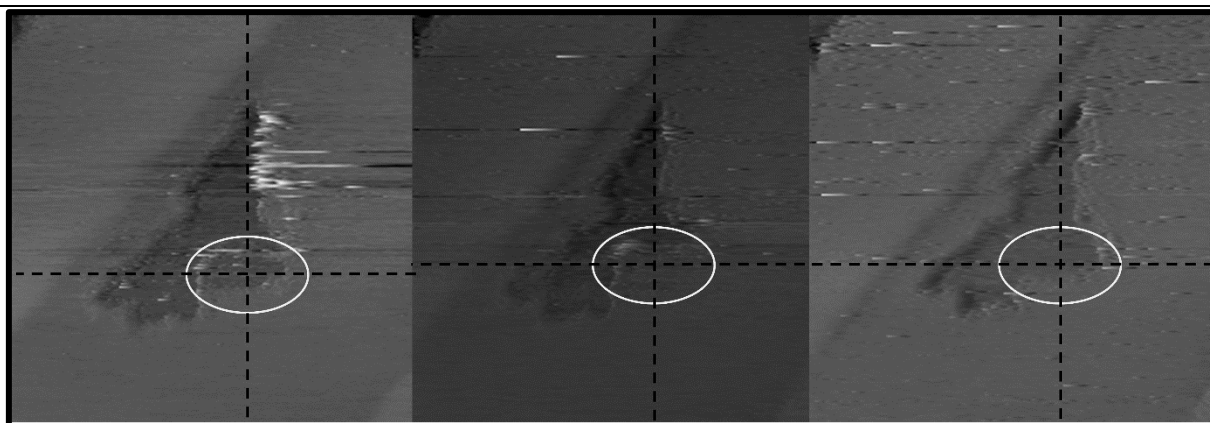
Fig 4.3.2 – STM measurements of CeO$_2$ at respectively 2V, 2.5V and 3V. The white ellipses indicate a region of electronic contrast between different voltages.

To analyze the results of purely the wavelet denoise, the images at 1V and 3V were chosen to carry out the process. Color scale was added to them through the usage of Gwyddion SPM analysis software [41]. In addition to the color scale, the images were treated by standard SPM community methods such as leveling the data, aligning rows, correcting horizontal scars and removing height displacement background. After these steps wavelet noise reduction was applied. The wavelet denoise used Symlet4 as a mother wavelet, at level 5 decomposition, with soft adaptative thresholding. The results are depicted in Fig. 4.3.3. The wavelet transform denoising was performed separately, i.e., all four images in Fig. 4.3.3 have been treated in Gwyddion as described above, but only the two images in the right column were processed using wavelet denoising method. Fig. 4.3.3 is then similar to Fig. 4.2.4, allowing one to see the results of a pure wavelet denoising.
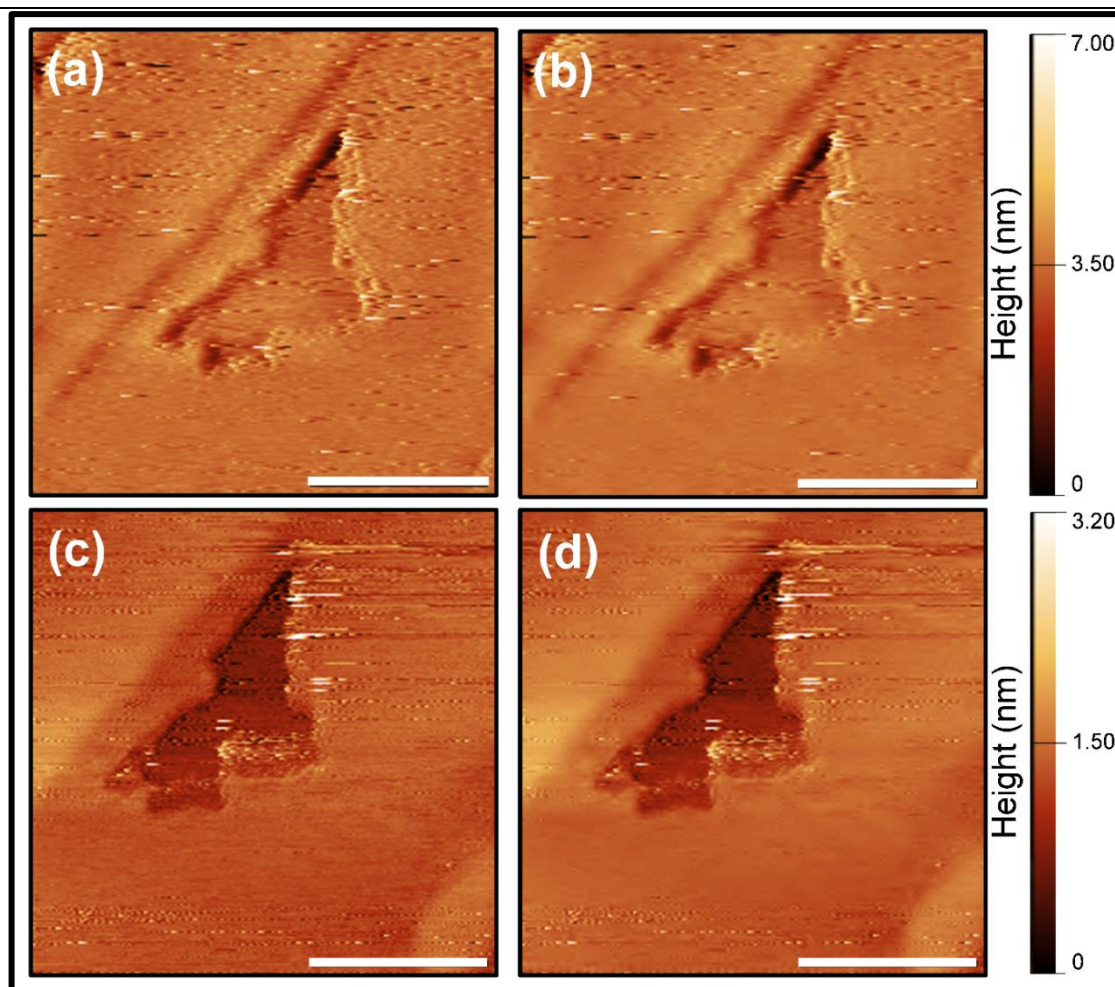
Fig 4.3.3 – Results on wavelet denoising. a) CeO_2 STM image at 3V bias without wavelet denoising. b) CeO_2 STM image at 3V bias with wavelet denoising. c) CeO_2 STM image at 1V bias without wavelet denoising. d) CeO_2 STM image at 1V bias with wavelet denoising. The scalebar is 20nm.

To better visualize the effects of the wavelet treatment performed, topographic profiles are extracted from Fig. 4.3.4, as in the method calibration chapter. It is possible to observe similar results compared to the method calibration data, indicating that the process was effective. The oscillating pattern is attenuated as expected, while the main peaks keep their form.
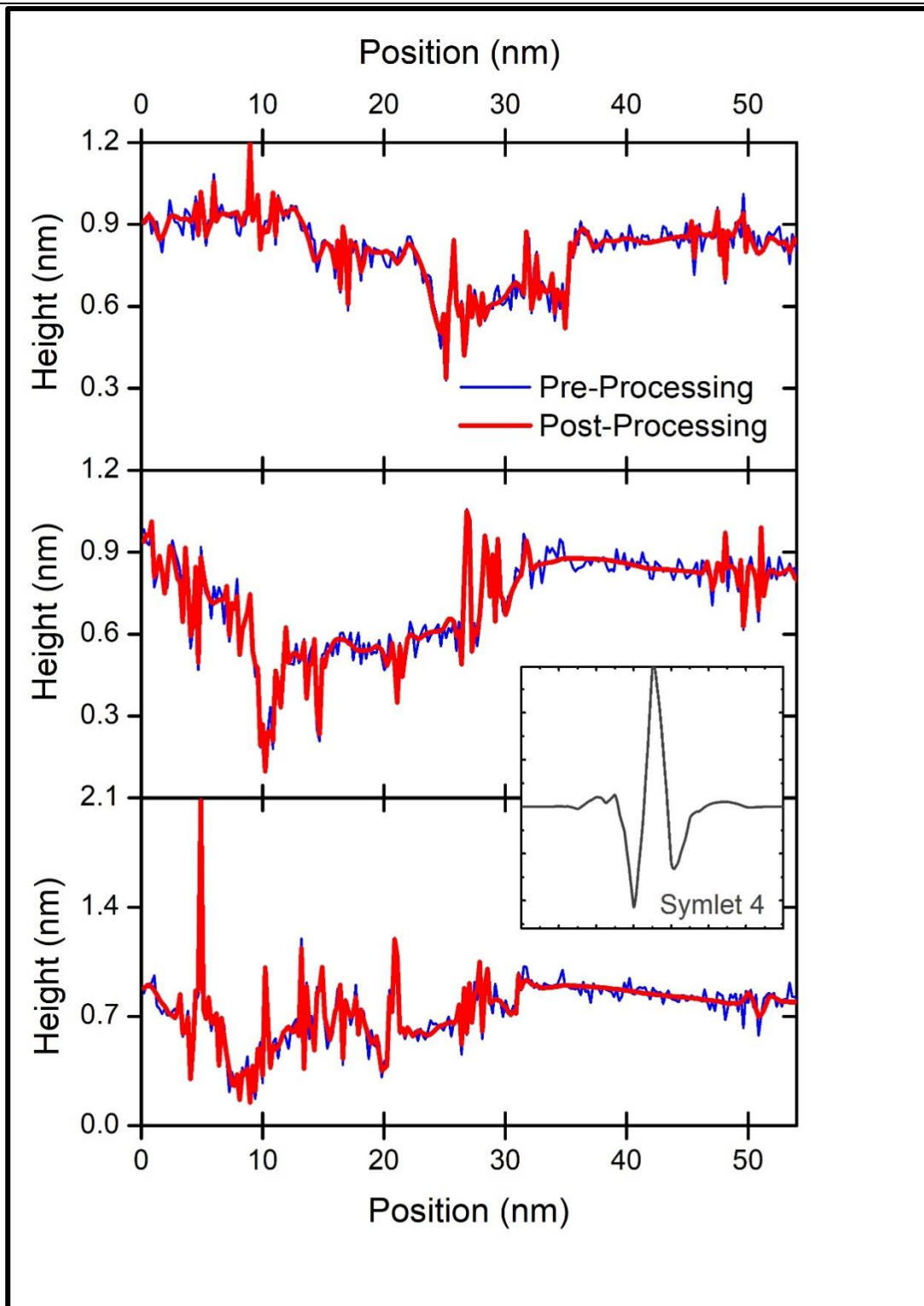
Fig. 4.3.4 – Three topographic vertical profiles extracted randomly from Fig. 4.3.3 depicting the results after the denoising.

To study the difference of processing the images with wavelets, in respect to the voltage contrast, the 2.5V bias image from Fig. 4.3.1 was also used. Vertical and horizontal

profiles were extracted along the black dotted line, indicated in Fig. 4.3.2. The position of these profiles is crucial, as they are placed to extract information from the region where the contrast between distinct voltages is observed. From Fig. 4.3.5 it is already possible to observe that the contrast seems to be easier to visualize in profiles.
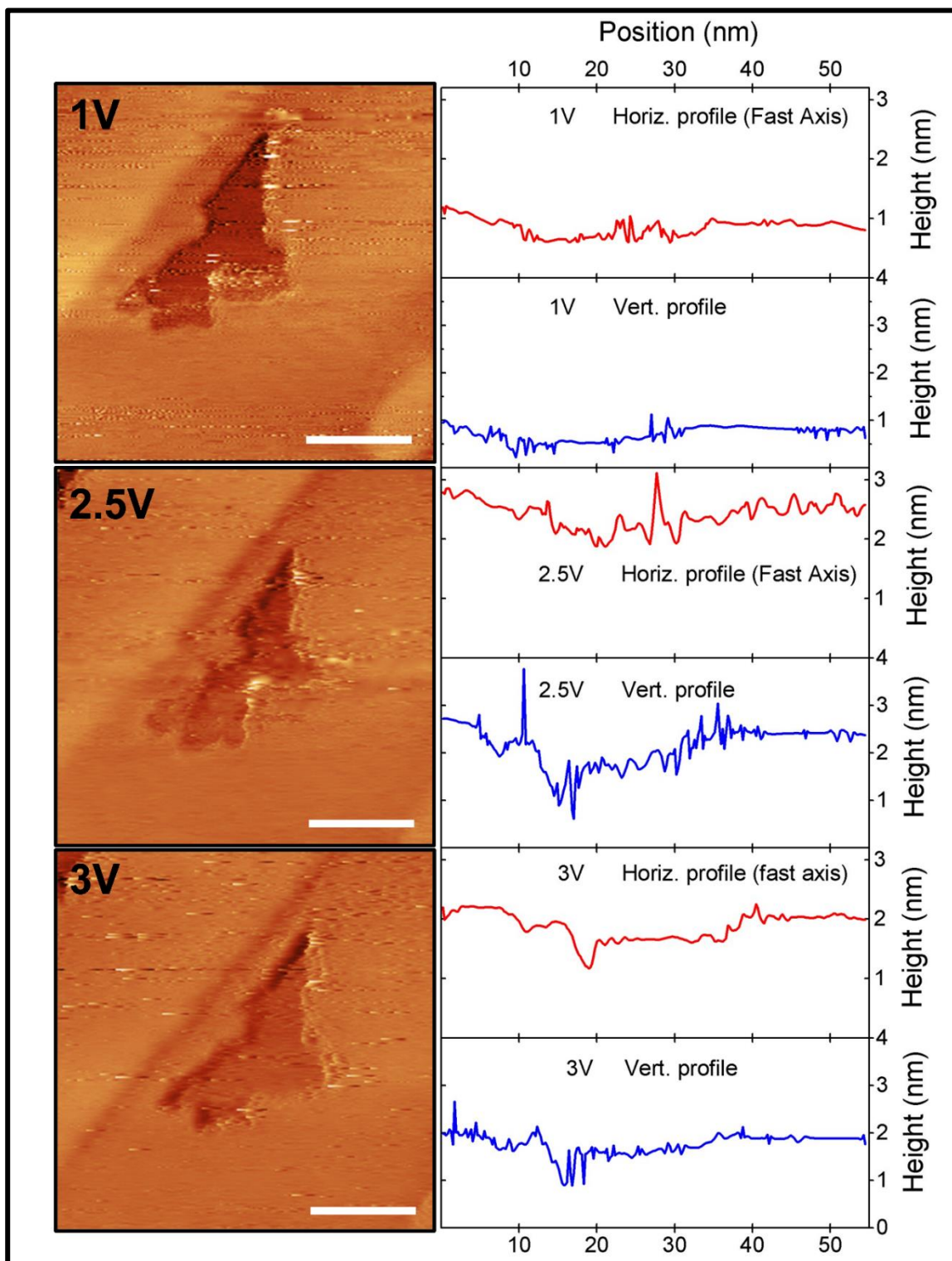
Fig. 4.3.5 – STM images of CeO_2 at different tensions (left) and plot of vertical and horizontal topographic profiles along the dotted lines (right). The profiles were extracted from the lines indicated in Fig. 4.3.2.

      The next step is to compare, in combined visualization, two profiles at different voltages. For this, the vertical profiles of the 1V bias and the 2V bias image are plotted together (see Fig.4.3.6). The 1V profile is shifted to equalize the height of the substrate, and the contrast in the nanostructure is greatly evidenced. This is done relying on the fact that HOPG is a very stable substrate, with little reaction to bias variation in the used range if compared to CeO_2.

Fig. 4.3.6 – Comparison between the vertical profiles of the 1V bias and the 2.5V bias image. The vertical profiles were extracted respectively in the delimited vertical lines in the STM image at the top of the figure.

Different than expected, the contrast is more pronounced in the rest of the nanostructure rather in the region of interest (white ellipses). However, there is still relevant information in the region of interest. The same is observed between 1V profile and 3V profile, depicted in Fig. 4.3.7. Again, the 1V profile is shifted to equate the height of the substrate. Nevertheless, there is more contrast in the region of interest for Fig. 4.3.7. A better form to visualize the difference of contrast between the nanostructure and the substrate region is to subtract one profile from another. The resulting function would be approximately zero for the substrate region, and non-zero for the nanostructure region.
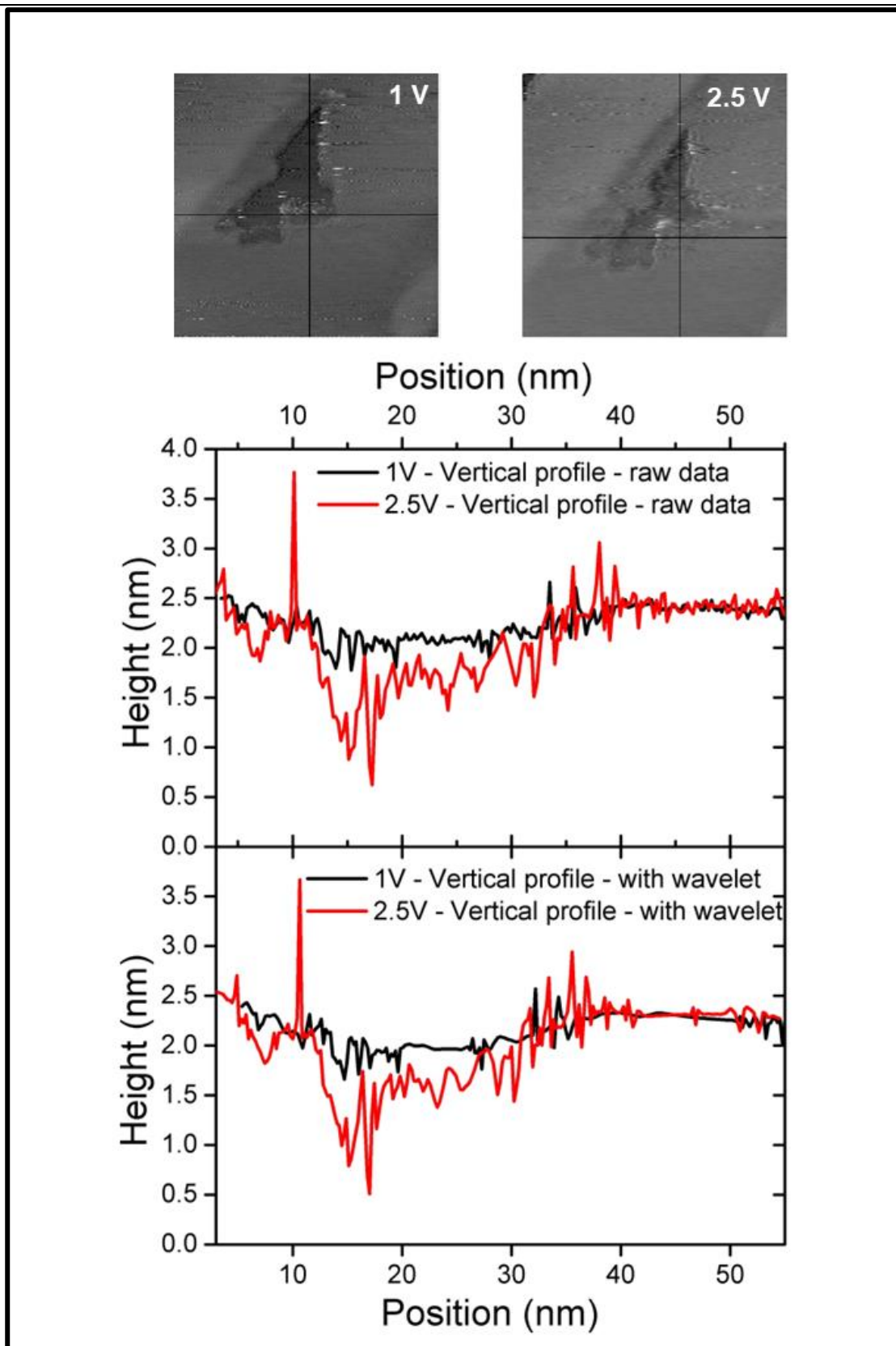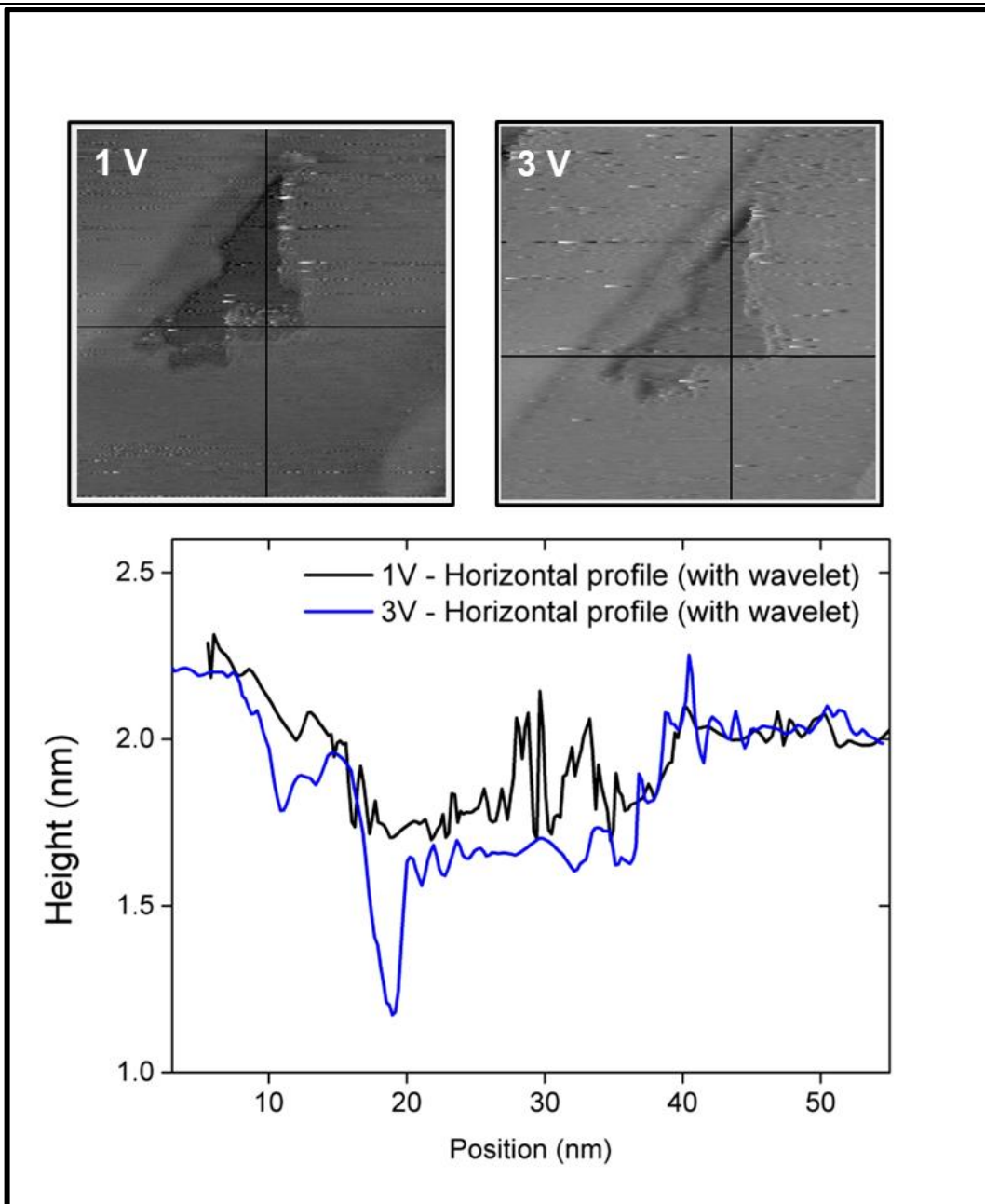
Fig. 4.3.7 – Comparison between the vertical profiles of the 1V bias and the 3V bias image. The profiles were extracted respectively in the delimited horizontal lines in the STM images at the top of the figure.

Fig. 4.3.8 – Contrast between 1V profile and 2V profile with wavelet (top) and without wavelet (bottom).

Doing so, we obtain Fig. 4.3.8. It is possible to see the expected result, values oscillating between zero for the substra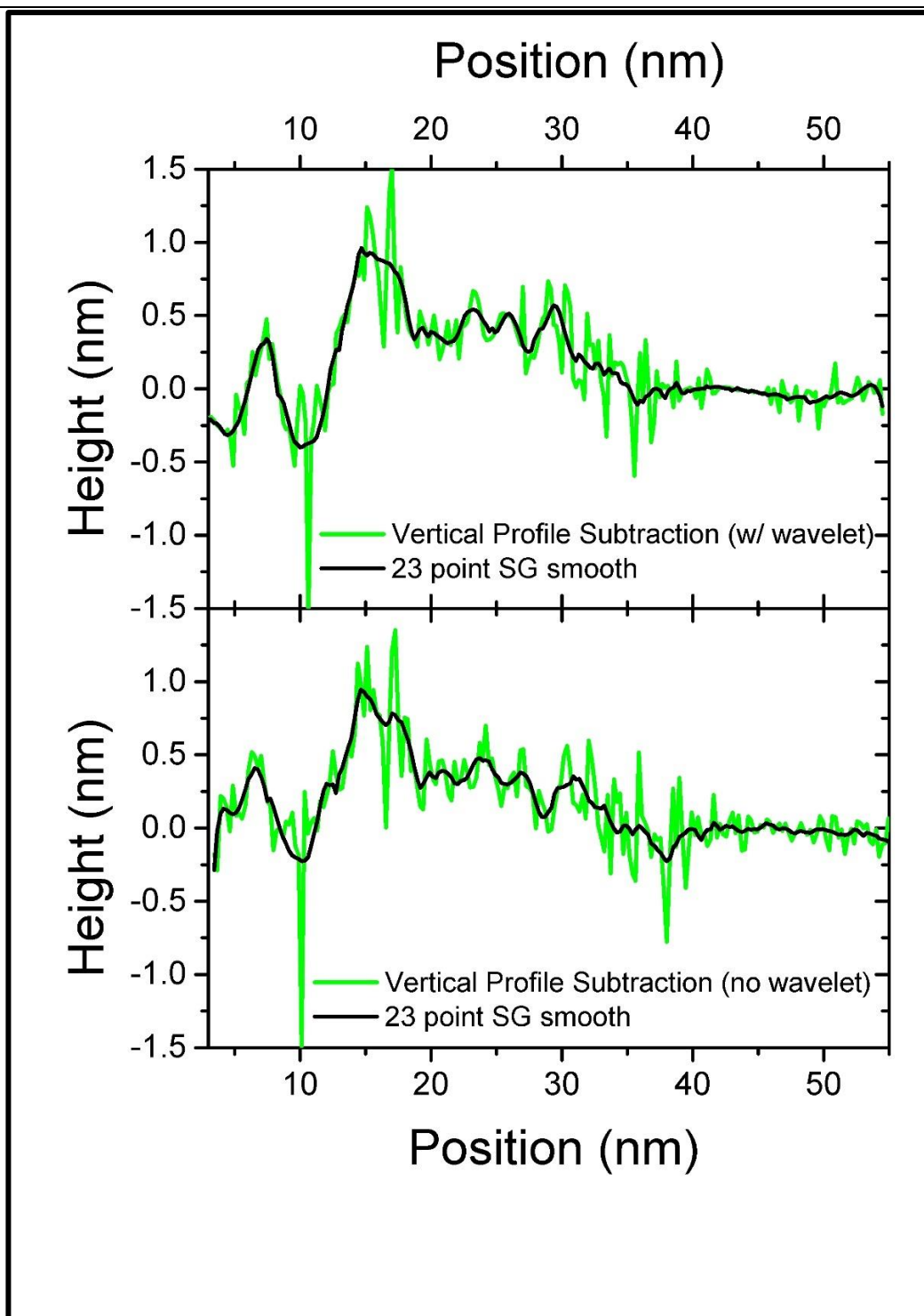te region, and non-zero values for the nanostructure region. This clearly indicates that there is little to no contrast between two different tensions

in the substrate region. At the same time, Fig. 4.3.8 also indicates a significative contrast in the region of the CeO_2 nanostructure.

The wavelet denoising method is then used to accentuate weak spectroscopic contrast. This becomes clear when we compare Fig. 4.3.8 (top) with Fig. 4.3.8 (bottom). It is possible to observe the contrast line dropping to zero slightly faster for the process performed without the wavelet denoising. Another important observation is the signal oscillates less for the wavelet treated image. This strongly suggests that it is possible to obtain a higher and clear spectroscopic signal by processing the data through the use of wavelets.

Since line profiles show a clear gain in data quality using wavelet one can proceed to two-dimensional data treatment and subsequent processes in order to provide improved data visualization. Figure 4.3.9 shows differences of STM data from normalized images measured in distinct applied bias. In this case the STM data is leveled at the HOPG substrate regions (such as in figures 4.3.6 and 4.3.7) and evidences regions in which the relative number of available electronic states has increased from the lower to the higher bias.
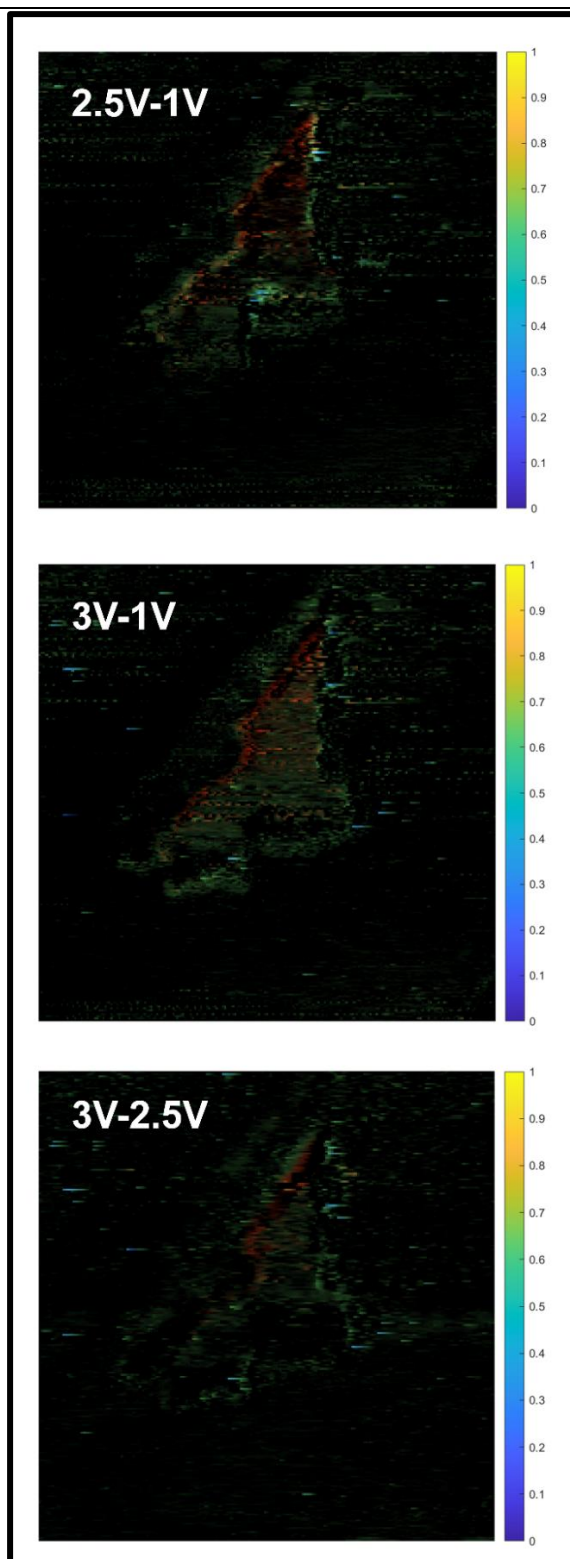
Fig. 4.3.9 – Differences of wavelet-processed STM images, leveled at the substrate region (shown in black). The upper panel shows the relative electronic state filling that takes place between 2.5V and 1V, with a concentration of color-enhanced regions around the CeO2 nanostructure (possibly due to the presence of edge states). The middle panel shown a similar electronic contrast map, between 3V and 1V, where a more homogeneous filling is

observed. Finally, the lower panel shows the contrast map built between 3V and 2.5V, indicating that electronic states at the center/upper region of the nanostructure may be bulk-like and are filled in this bias interval.

The upper panel, where 2.5V − 1V data is shown, clearly exhibits enhanced colored contours around the CeO2 nanostructure. Indicating that edge states are filled between 1 V and 2.5 V. These states may be related to vacancies, defects and impurities that are only mildly present at the nanostructure center. A similar contrast map built between 3V and 1V STM data shows a more homogeneous color distribution as one moves along the nanostructure area, showing that homogeneous spatial state filling takes place within the 3V bias range. A complementary contrast map (lower panel of fig. 4.3.9) extracted from 3V - 2.5V datasets clearly shows more prominent colored zones at the center/upper part of the nanostructure indicating that electronic states filled in the 2.5V − 3V range may belong to bulk bands of CeO2 structure.

Finally, in order to understand the gain obtained by analyzing wavelet-treated datasets with electronic contrast, figure 4.3.10 shows the residual noise extracted from the subtraction of 1V STM maps with and without wavelet process. One observes that most of the noise is concentrated within the nanostructure area, showing that the dataset stabilization is more pronounced inside the CeO2 nanostructure, as initially desired.
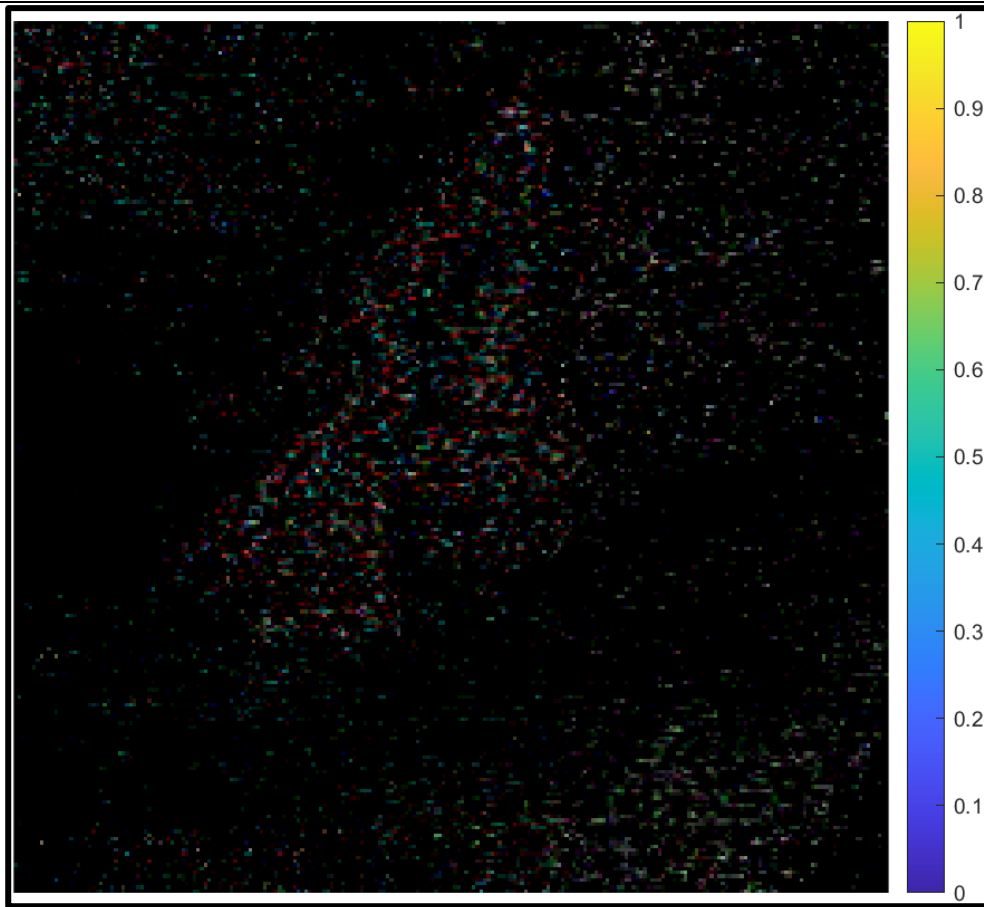
Fig. 4.3.10 – Map of extracted STM noise using wavelet method, obtained from the difference of 1V maps generated with and without wavelet processing. The result indicates a more pronounced noise suppression inside the nanostructure.

5. CONCLUSIONS AND PERSPECTIVES

In this work, we gathered evidence that strongly indicates the use of wavelet transforms as a good technique to enhance weak spectroscopic contrast in Scanning Tunneling Microscope images. The treatment relies mainly in noise reduction through the use of thresholding. To detect the values of threshold, an automatic image-dependent method (fixed-form threshold) was utilized. A mother-wavelet (Symlet4, chosen through trial and error) is used to evince different frequencies that compose the original STM image, allowing us to filter unwanted frequencies. This process results in a cleaner image, with less random oscillations between the adjacent pixels.

To test and calibrate the method, we proposed a four-step evaluation using two distinct images. The four-steps consist of, visual analysis, topographic profile extraction and analysis, Fourier Transform analysis and residual map analysis. This method was used to study the results of the wavelet denoise using the two test images. Each step revealed advantages of the method, as well as some minor concerns related to data processing techniques in general. The advantages revealed in the steps are a good indication that the method is indeed reliable for the utilization we propose.

The method was then used to process STM images of a Cerium Oxide nanostructure in different tensions. We have successfully show that by suppressing this noise, it is possible to obtain a higher and cleaner contrast when subtracting two STM images with different tensions. This is of extreme importance since these results indicates that the technique may be useful to extract more electronic information from the so commonly used STM.

The discoveries of this work have been condensed in a MATLAB code. The code allows the user load a common output file for the STM software (.csv), construct a visual matrix to see the image, perform the wavelet noise reduction and see the results. The user can also change the parameters of the process to better adapt to each individual study. The MATLAB code is available in the Appendix - A.

References

[1] Thiago C. Ribeiro, Rafael Reis, Daniele C. Ferreira, Douglas R. Miquita, Guilherme A.S. Ribeiro, Mario S.C. Mazzoni, Angelo Malachias, Thais Chagas, Rogerio Magalhaes-Paniago, Applied Surface Science **591**, 153153 (2022).

[2] A. Graps, "An introduction to wavelets," in IEEE Computational Science and Engineering, vol. **2**, no. 2, pp. 50-61, (1995).

[3] Rioul, O., & Vetterli, M., "Wavelets and signal processing". IEEE Signal Processing Magazine, **8**(4), 14–38, (1991).

[4] Christopher Torrence, Gilbert P. Compo, "A Practical Guide to Wavelet Analysis", Vol. **79**, No. 1, (1998).

[5] Treil, Nicolas, Stephane Mallat, and Ruzena Bajcsy. "Image wavelet decomposition and applications". No. MS-CIS-89-22. (1989).

[6] Huiying, Liang, Lukkarinen Sakari, and Hartimo Iiro. "A heart sound segmentation algorithm using wavelet decomposition and reconstruction." In Proceedings of the 19th Annual International Conference of the IEEE Engineering in Medicine and Biology Society.'Magnificent Milestones and Emerging Opportunities in Medical Engineering'(Cat. No. 97CH36136), vol. **4**, pp. 1630-1633. IEEE, (1997).

[7] Kingsbury, N., Magarey, J., "Wavelet Transforms in Image Processing". In: Procházka, A., Uhlíř, J., Rayner, P.W.J., Kingsbury, N.G. (eds) Signal Analysis and Prediction. Applied and Numerical Harmonic Analysis. Birkhäuser, Boston, MA. (1998).

[8] Jonathan N. Bradley, Christopher M. Brislawn, and Thomas Hopper "FBI wavelet/scalar quantization standard for gray-scale fingerprint image compression", Proc. SPIE 1961, Visual Information Processing II, (1993).

[9] Demirel, H., & Anbarjafari, G., "IMAGE Resolution Enhancement by Using Discrete and Stationary Wavelet Decomposition". IEEE Transactions on Image Processing, **20**(5), 1458–1460. (2011).

[10] Vilimek, Dominik, et al. "Comparative analysis of wavelet transform filtering systems for noise reduction in ultrasound images." Plos one 17.7 (2022): e0270745.

[11] Chen, G. Y., Bui, T. D., & Krzyzak, A., "Image denoising using neighbouring wavelet coefficients". Integrated Computer-Aided Engineering, **12**(1), 99–107. (2005).

[12] Chang, S. G., Bin Yu, & Vetterli, M., "Adaptive wavelet thresholding for image denoising and compression". IEEE Transactions on Image Processing, **9**(9), (2000).

[13] Workman, Michael J., et al. "Application of the discrete wavelet transform to SEM and AFM micrographs for quantitative analysis of complex surfaces." Langmuir **31**.17, (2015).

[14] Wu, Y., Fang, Y., Ren, X., & Lu, H., "A Wavelet-Based AFM Fast Imaging Method With Self-Tuning Scanning Frequency". IEEE Transactions on Nanotechnology, **16**(6), 1088–1098. (2017).

[15] Benítez, R., & Bolós, V. J., "Searching events in AFM force-extension curves: A wavelet approach". Microscopy Research and Technique, **80**(1), 153–159. (2016).

[16] V Pukhova and G Ferrini, IOP Conf. Ser.: Mater. Sci. Eng. **256**, (2017).

[17] Schimmack, M., & Mercorelli, P., "A Wavelet Packet Tree Denoising Algorithm for Images of Atomic-Force Microscopy". Asian Journal of Control, **20**(4), (2018).

[18] Carmichael, Matt, et al. "Using wavelets to analyze AFM images of thin films: Surface micelles and supported lipid bilayers." Langmuir **20**.26, (2004).

[19] Wang, Zhenyu, et al. "Wavelet analysis of higher harmonics in tapping mode atomic force microscopy." Micron **118** 58-64, (2019).

[20] Messer, P. K., et al. "A multiscale wavelet algorithm for atom tracking in STM movies." New Journal of Physics **24**.3 (2022).

[21] Bui, Kevin, et al. "Segmentation of scanning tunneling microscopy images using variational methods and empirical wavelets." Pattern Analysis and Applications **23**, 625-651, (2020).

[22] Gackenheimer, C., Cayon, L., & Reifenberger, R., "Analysis of scanning probe microscope images using wavelets". Ultramicroscopy, **106**(4-5), 389–397, (2006).

[23] Maksumov, A., Vidu, R., Palazoglu, A., & Stroeve, P., "Enhanced feature analysis using wavelets for scanning probe microscopy images of surfaces". Journal of Colloid and Interface Science, **272**(2), 365–377, (2004).

[24] Tkal', V. A., et al. "Wavelet processing of nanocomposite images obtained by scanning tunnel and electron microscopes." Inorganic Materials, **46**, 1555-1557, (2010).

[25] Xu, Lijun, et al. "Two-in-One Implementation of Noise Reduction and Incline Emendation for Atomic Force Microscopic Images." IEEE Instrumentation and Measurement Technology Conference, (2008).

[26] Homeniuk, Darren, Marek Malac, and Misa Hayashida. "Wavelet transform-based electron tomography measurement of buried interface roughness." Ultramicroscopy **194**, 64-77, (2018).

[27] Payam, Amir Farokh, et al. "Data acquisition and imaging using wavelet transform: a new path for high speed transient force microscopy." Nanoscale Advances **3**.2, 383-398, (2021).

[28] Rekhviashvili, S. Sh. "Wavelet-transform processing of images in atomic force microscopy." Technical Physics Letters **28**, 237-238, (2002).

[29] Oliveira, J. P., Bragança, A., Bioucas-Dias, J., Figueiredo, M., Alcácer, L., Morgado, J., & Ferreira, Q., "Restoring STM images via Sparse Coding: noise and artifact removal". (2016).

[30] G. Binnig, H. Rohrer, C. Berber, and E. Weibel, Appl. Phys. Lett. **40** (2), 178 (1981).

[31] C. Julian Chen, "Introduction to Scanning Tunneling Microscopy". Oxford University Press, Third edition, (2021).

[32] Meyer, E., Hug, H.J., Bennewitz, R., "Introduction to Scanning Probe Microscopy". In: Scanning Probe Microscopy. Advanced Texts in Physics. Springer, Berlin, Heidelberg. (2004).

[33] Zhang, Wei, et al. "First steps of blue phosphorene growth on Au (1 1 1)." Materials Today: Proceedings **39**, 1153-1156, (2021).

[34] Chagas, M. Pelc, P. H. Gonçalves, I. Antoniazzi, J. W. González, A. Ayuela, J. M. J. Lopes, M. H.Oliveira, R. Magalhães-Paniago, and A. Malachias, "Self-assembled triangular graphene nanostructures: Evidence of dual electronic response", Carbon, vol. **142**, pp. 580–591, (2019).

[35] Alpichshev, Zhanybek, et al. "STM imaging of a bound state along a step on the surface of the topological insulator Bi 2 Te 3." Physical Review B **84**.4, 041104, (2011).

[36] Hus, Saban M., et al. "Detection of the spin-chemical potential in topological insulators using spin-polarized four-probe STM." Physical Review Letters **119**.13, 137202, (2017).

[37] Pettinger, Bruno, et al. "Surface-enhanced and STM-tip-enhanced Raman Spectroscopy at Metal Surfaces." Single Molecules **3**.5-6, 285-294, (2002).

[38] Kubby, Joel A., and John J. Boland. "Scanning tunneling microscopy of semiconductor surfaces." Surface science reports **26**.3-6, 61-204, (1996).

[39] Sumetskii, M., and A. A. Kornyshev. "Noise in STM due to atoms moving in the tunneling space." Physical Review B **48**.23, 17493, (1993).

[40] Möller, R., A. Esslinger, and B. Koslowski. "Thermal noise in vacuum scanning tunneling microscopy at zero bias voltage." Journal of Vacuum Science & Technology A: Vacuum, Surfaces, and Films **8**.1, 590-593, (1990).

[41] D. Necas and P. Klapetek, "Gwyddion: an open-source software for SPM data analysis", Central European Journal of Physics, vol. **10**, pp. 181–188, (2012).

[42] Sonka, Milan, Vaclav Hlavac, and Roger Boyle. "Image processing, analysis, and machine vision". Cengage Learning, (2014).

[43] Lin, Zhiyong, et al. "Flatbands and emergent ferromagnetic ordering in Fe3 Sn2 kagome lattices." Physical review letters **121**.9, 096401, (2018).

[44] IBM. "Scanning Tunneling Microscope – Overview". Available at:
https://www.ibm.com/ibm/history/ibm100/us/en/icons/microscope/#:~:text=In%201981%2

C%20two%20IBM%20researchers,scanning%20tunneling%20microscope%20(STM).
(Accessed: 16/06/2023)

[45] McIntyre, David H. "Quantum mechanics". Cambridge University Press, (2022).

[46] Workshop Nonscience on the Tip, "Scanning Tunneling Microscopy and Spectroscopy", NUE UNIQUE, University of Washington.

[47] Silva, Thaís Chagas Peixoto, A. A. (2020). "Tunneling spectroscopy of 2D materials: unraveling their density of states and the relationship with local atomic environment". 154f., enc. : [Doctoral thesis/Federal University of Minas Gerais]

[48] Michel, Carlos R., and Alma H. Martínez-Preciado. "CO sensor based on thick films of 3D hierarchical CeO2 architectures." Sensors and Actuators B: Chemical 197 (2014): 177-184.

[49] Sun, Q., Du, J., Tian, L., Wu, J., & Zhang, X. (2021). Detection of organophosphorus pesticides: exploring oxime as a probe with improved sensitivity by CeO2-modified electrode. Analytical Methods, 13(39), 4634-4641

[50] Al-Kuhaili, M. F., Durrani, S. M. A., & Bakhtiari, I. A. (2010). Carbon monoxide gas-sensing properties of CeO2–WO3 thin films. Materials Science and Technology, 26(6), 726-731.

[51] Jiang, F., Wang, S., Liu, B., Liu, J., Wang, L., Xiao, Y., ... & Liu, X. (2020). Insights into the influence of CeO2 crystal facet on CO2 hydrogenation to methanol over Pd/CeO2 catalysts. ACS Catalysis, 10(19), 11493-11509.

[52] Montini, T., Melchionna, M., Monai, M., & Fornasiero, P. (2016). Fundamentals and catalytic applications of CeO2-based materials. Chemical reviews, 116(10), 5987-6041.

[53] Yang, C., Lu, Y., Zhang, L., Kong, Z., Yang, T., Tao, L., ... & Wang, S. (2021). Defect Engineering on CeO2-Based Catalysts for Heterogeneous Catalytic Applications. Small Structures, 2(12), 2100058.

[54] Chen, X., Gao, S., Wang, H., Liu, Y., & Wu, Z. (2011). Selective catalytic reduction of NO over carbon nanotubes supported CeO2. Catalysis Communications, 14(1), 1-5.

[55] Melchionna, M., Bevilacqua, M., & Fornasiero, P. (2020). The electrifying effects of carbon-CeO2 interfaces in (electro) catalysis. Materials Today Advances, 6, 100050.

[56] Joung, D., Singh, V., Park, S., Schulte, A., Seal, S., & Khondaker, S. I. (2011). Anchoring ceria nanoparticles on reduced graphene oxide and their electronic transport properties. The Journal of Physical Chemistry C, 115(50), 24494-24500.

[57] Zhang, L., Fang, Q., Huang, Y., Xu, K., Chu, P. K., & Ma, F. (2018). Oxygen vacancy enhanced gas-sensing performance of CeO2/graphene heterostructure at room temperature. Analytical chemistry, 90(16), 9821-9829.

[58] Naganaboina, V. R., & Singh, S. G. (2021). Graphene-CeO2 based flexible gas sensor: Monitoring of low ppm CO gas with high selectivity at room temperature. Applied Surface Science, 563, 150272.

[59] Zhang, L., Fang, Q., Huang, Y., Xu, K., Chu, P. K., & Ma, F. (2018). Oxygen vacancy enhanced gas-sensing performance of CeO2/graphene heterostructure at room temperature. Analytical chemistry, 90(16), 9821-9829.

[60] Krebs, H. U., Weisheit, M., Faupel, J., Süske, E., Scharf, T., Fuhse, C., ... & Buback, M. (2003). Pulsed laser deposition (PLD) - a versatile thin film technique. Advances in solid state physics, 505-518.

[61] Christen, H. M., & Eres, G. (2008). Recent advances in pulsed-laser deposition of complex oxides. Journal of Physics: Condensed Matter, 20(26), 264005.

[62] Choudhury, B., & Choudhury, A.. "Ce3+ and oxygen vacancy mediated tuning of structural and optical properties of CeO2 nanoparticles". Materials Chemistry and Physics, 131(3), 666–671, (2012).

[63] Shannon, Robert D. "Revised effective ionic radii and systematic studies of interatomic distances in halides and chalcogenides." Acta crystallographica section A: crystal physics, diffraction, theoretical and general crystallography 32.5 (1976): 751-767.

[64] Materials Project. "CeO2 mp-20194". Available at: https://next-gen.materialsproject.org/materials/mp-20194. (Accessed: 07/14/2023)

[65] Nörenberg, H., & Harding, J. H. "The surface structure of CeO2(001) single crystals studied by elevated temperature STM". Surface Science, 477(1), 17–24. (2001).

[66] Younis, A., Chu, D., & Li, S.. "Cerium Oxide Nanostructures and their Applications". Functionalized Nanomaterials. (2016).

Appendices

APPENDIX A – MATLAB code

```matlab
%%
%Primera parte: Lê o arquivo CSV, separa em 3 colunas (x,y,z), organiza os
%dados no formato de uma matriz imagem/visual e armazena essa matriz na
%posição 1 de uma célula.

clc;
close all;
clear;
num_imagens = 1;
%Número de imagens utilizadas
for a = 1:1:num_imagens
    filename = ['n' num2str(a,'%02d') '.csv'];                          %Nome
da série de arquivos
    A = readmatrix(filename);                                           %Lê o
arquivo csv
    for i = 1:1:length(A)
        eixox(i) = A(i,1);
        eixoy(i) = A(i,2);
%Separa o arquivo csv em x y e z
        z(i) = A(i,3);
    end
    tam = sqrt(length(z));
    contador=1;
    for cy=1:tam
        for cx=1:tam
            zfinal(((tam+1)-cy),cx) = z(contador);
%Transforma o arquivo csv em uma matriz visual
            contador = contador + 1;
        end
    end
    cel{num_imagens} = zfinal;
%Armazena a matriz em uma célula
    I = mat2gray(zfinal);
%Transforma a matriz em uma imagem em escala cinza
    imwrite(I, ['testewavelet' num2str(a,'%02d') '.png'], 'png');       %Gera
uma imagem .tif a partir dos dados
    m1 = imread(['testewavelet' num2str(a,'%02d') '.png']);
%Armazena a imagem na variável m1
    figure(1)                                                           %Gera
figura(1) com a imagem gerada usando dados do arquivo 1
    imshow(m1);
    [dm1,a2,a3] = func_denoise_dw2d(m1);
%Realiza a redução de ruído usando wavelet
    figure(2)                                                           %Gera
a figura(2) com a imagem após o tratamento
    imshow(dm1);
    r = round(1 + (tam-1) .* rand(1,1));
    for n=1:1:(length(m1))
        perfilverticalpreproc(n) = m1(40,n);
    end
    for n=1:1:(length(m1))
        perfilhorizontalpreproc(n) = m1(n,206);
    end
%Extração de perfis verticais e horizontais antes e depois do tratamento
```

```matlab
    for n=1:1:(length(m1))
        perfilverticalposproc(n) = dm1(40,n);
    end
    for n=1:1:(length(m1))
        perfilhorizontalposproc(n) = dm1(n,206);
    end
    figure(3)                                              %Gera
figura(3) comparando perfis antes e depois do processamento
    subplot(2,1,1), plot(perfilhorizontalpreproc,'b');
    subplot(2,1,2), plot(perfilhorizontalposproc,'r');
    sub = dm1 - m1;
%Subtrai a imagem antes e depois pra observarmos o resíduo
    figure(4)
    imshow((mat2gray(sub)))
end
%%
%Segunda parte: É realizada uma análise do resultado usando Transformada de
%Fourier (Fast Fourier Transform)
eixoreal = linspace(0,max(z),512);                         %É
criado um vetor para manter real a escala do eixo x, deve ser alterado
figure(1)
%Figura(1) mostra os perfis antes e depois do processamento
subplot(3,1,1), plot(eixoreal,perfilhorizontalpreproc,'b'),xlabel('m');
subplot(3,1,2), plot(eixoreal,perfilhorizontalposproc,'r'),xlabel('m');
subplot(3,1,3), plot(eixoreal,perfilhorizontalpreproc,'b'),xlabel('m')
hold on
plot(eixoreal,perfilhorizontalposproc,'r'), legend('Pre-processing','Post-
processing');
fs = 640;
%Frequência de amostragem
t = 0:1/fs:10-1/fs;                                        %10
second span time vector
fftSIG = fft(perfilhorizontalpreproc);
fftsigfinal = fft(perfilhorizontalposproc);
n = length(perfilhorizontalpreproc);
%number of samples
f = (0:n-1)*(fs/n);
%frequency range
power = abs(fftSIG).^2/n;                                  %power
of the DFT
power2= abs(fftsigfinal).^2/n;
y0 = fftshift(fftSIG);                                     %shift
y values
y1 = fftshift(fftsigfinal);
f0 = (-n/2:n/2-1)*(fs/n);                                  %0-
centered frequency range
power0 = abs(y0).^2/n;                                     %0-
centered power
power3 = abs(y1).^2/n;
figure(3)
%Figura(3) mostra FFT em escala do perfil antes e depois do processamento
subplot(2,1,1), plot(f0,log(power0))
xlabel('Frequency(Hz)')
ylabel('Log(Power)')
subplot(2,1,2), plot(f0,log(power3),'r')
xlabel('Frequency(Hz)')
ylabel('Log(Power)')
%%
```

```matlab
function [XDEN,cfsDEN,dimCFS] = func_denoise_dw2d(X)
%Função de redução de ruído através de decomposição em wavelet
wname = 'sym4';                                                    %Tipo
de wavelet usado
level = 4;                                                         %Level
de decomposição wavelet
[C,S]= wavedec2(X,level,wname);
%Decomposição wavelet
thr = wthrmngr('dw2ddenoLVL','sqtwolog',C,S,'one');
%Determinação de threshold
sorh = 's';
%Escolha de soft ou hard thresholding
roundFLAG = true;
[coefs,sizes] = wavedec2(X,level,wname);
[XDEN,cfsDEN,dimCFS] = wdencmp('lvd',coefs,sizes, ...
    wname,level,thr,sorh);
if roundFLAG , XDEN = round(XDEN); end
if isequal(class(X),'uint8') , XDEN = uint8(XDEN); end
end
```